NTNU – Trondheim
Norwegian University of
Science and Technology

Effect of CuO doping in Bi0.5K0.5TiO3

Development of Lead-Free Ferroelectric
Materials

Duy Quang Che

Chemical Engineering and Biotechnology
Submission date: June 2015
Supervisor: Tor Grande, IMTE
Co-supervisor: Espen Wefring, IMT

Norwegian University of Science and Technology
Department of Materials Science and Engineering

Preface

I hereby declare that the work presented in this document has been performed independently and in accordance with the rules and regulations of the Norwegian University of Science and Technology (NTNU).

This thesis presents the work carried out at the Department of Material Science and Engineering at the Norwegian University of Science and Technology (NTNU), spring 2015, under the supervision of Professor Tor Grande, with co-supervision from Ph.D candidate Espen Tjønneland Wefring.

Trondheim, June 25, 2015
Duy Che

Acknowledgments

First of all I would like to express my gratitude to my main supervisor, Tor Grande, for the guidance and encouragement he has provided during this work. I have always appreciated our weekly meetings and his support has been invaluable. Additionally I have been fortunate to have an excellent co-supervisor, Espen Wefring, who has taken time to answer high and low level questions and spending many hours helping me in the laboratory. I would also like to thank all the members in the ferro group for many good advices as well as interesting presentations and discussions. Another thanks goes to my family for always believing in me and supporting me. I also have to thank Ingrid Nyeng for reading through my thesis and giving me invaluable feedback. Finally, I would like to express my gratitude to everyone that has made the past 6 years an unforgettable experience.

Abstract

Piezoelectric materials are currently used in a significant number of electronic applications, and lead-free piezoelectric materials have obtained much attention in the recent years. Bismuth potassium titanate, $Bi_{0.5}K_{0.5}TiO_3$ (BKT), is a lead-free piezoelectric alternative which has been studied with promising results. However, dense and phase pure BKT has proven to be challenging to prepare by the conventional solid state synthesis. This problem is often accredited to the volatility of A-site cations during high temperature sintering.

In this study, BKT ceramics with 0.0 - 2.0 mol% of excess A cations, and 0.3 - 0.9 mol% of CuO addition (BKTC-x, $x = 0.3 - 0.9$), have been prepared by the conventional solid state synthesis. The materials were investigated with respect to A to B stoichiometry, phase purity, density, dielectric and piezoelectric properties.

The nominal stoichiometric BKT is found to contain B-rich secondary phases. The material proves to be A cation deficient, as these secondary phases are removed by adding 2 mol% of excess A cations. The densities of these ceramics are measured to be about 92 % of theoretical density. The addition of CuO as a sintering aid was observed to be effective, as the relative density of CuO doped ceramics are determined to be above 95 %. The tetragonal perovskite structure are obtained for all investigated materials, where the lattice parameters slightly increase with increasing dopant level. The dielectic measurements confirms relaxor-like behavior for all compositions, as a broadening of the relative permittivity maximums are observed at the ferroelectric to paraelectric phase transition. In addition, the corresponding temperatures of the relative permittivity maximums decrease with decreasing frequency. The relative permittivity of the CuO doped materials are also found to be larger than the undoped BKT material. BKTC-0.9 provides the most open polarization-electric field hysteresis curve, as well as the largest maximum polarization of 8.5 $\mu m/cm^2$, indicating depinning of the domain walls. It was observed that the B-rich secondary phases gradually redeveloped with increasing CuO-addition. The result of these investigations suggest that copper ions compensate A cation vacancies on A-site as well as substituting with titanium on B-sites.

Sammendrag

Piezoelektriske materialer har stor anvendelse og er mye brukt i dagens teknnologiske samfunn. Blyzirkonattitanat-baserte (PZT) keramer er det mest brukte materialet i dagens marked, men på grunn av det høye blyinneholdet ønskes det av miljøhensyn å erstatte disse materialene med blyfrie alternativer. Vismut kaliumtitanat, $Bi_{0.5}K_{0.5}TiO_3$ (BKT), er et blyfritt piezoelektrisk material som har vært studert med lovende resultater. Dessverre har det vist seg vanskelig å produsere tette og faserene BKT med den konvensjonelle faststoffsyntesen. Tidligere artikler har knyttet dette problemet med høy flyktighet av A-kationer ved høy sintringstemperatur.

I denne oppgaven ble BKT-materialer med 0.0 - 2.0 mol% overskudd av A-kationer, og 0.3 - 0.9 mol% CuO-doping (BKTC-x, $x = 0.3 - 0.9$) framstilt ved den konvensjonelle faststoffsyntesen. Materialene ble utforsket med hensyn på A til B støkiometri, faserenhet, massetetthet, dielektriske og piezoelektriske egenskaper.

Det nominelle støkiometriske BKT-forbindelsen ble framstilt med B-rike sekundærfaser. Sekundærfasene blir fjernet ved å tilsette 2 mol% overskudd av A-kationer. Disse forbindelsene oppnår en tetthet tilsvarende 92 % av den teoretiske massetettheten.

Det blir observert at tilsetningen av CuO som sintringsmiddel er effektivt, ettersom massetettheten av BKTC-0.6 øker til 96 %. Den strukturelle karakteriseringen viser at alle materialene har tetragonal struktur, med økende gitterparametere som en funksjon av økende mengde CuO-doping. Dielektriske målinger antyder relaxorlignende oppførsel for alle materialene. Det blir observert brede relativ permitivitetmaksimaer ved den ferro- og paraelektriske faseovergangen. Videre blir det observert at temperaturen til de relative permitivitetmaksimaene avtar med avtagende frekvens. Piezoelektriske målinger viser at BKTC-0.9 gir den mest åpne polarisering-elektrisk felt hystereseløkken med maksimal polarisering lik 8.5 $\mu m/cm^2$ i forhold til den mer lukkede hystereseløkken observert for BKTC-0.3 som har maksimal polarisering lik 7.1 $\mu m/cm^2$. Det blir observert at B-rike sekundærfaser gradvis økte med hensyn til økt CuO-doping.

Resultatene av disse undersøkelsene antyder at kobberioner kompenserer med A-kationvakanser på A-plass, samt substituerer med titan på B-plass.

Contents

List of acronyms

BFO	Bismuth ferrite, $BiFeO_3$
BKT	Bismuth potassium titanate, $Bi_{0.5}K_{0.5}TiO_3$
BKT-*x*	Bismuth potassium titanate, x is mol% excess K and Bi
BKTC-*x*	Bismuth potassium titanate, x is mol% CuO addition
BNT	Bismuth sodium titanate, $Bi_{0.5}Na_{0.5}TiO_3$
EDS	Energy dispersive X-ray spectroscopy
KNN	Sodium potassium niobate, $K_{0.5}N_{0.5}NbO_3$
MPB	Morphotropic phase boundary
PLZT	Lead lanthanium zirconate titanate
PZT	Lead zirconate titanate, $PbZr_xTi_{1-x}O_3$
PNR	Polar nanometer regions
SE	Secondary electrons
SEM	Scanning electron microscopy
XRD	X-ray diffraction

Chapter 1

Introduction

1.1 Background

The piezoelectric effect was first discovered by the french physicists Jacques and Pierre Curie in 1880, when they observed that certain single-crystal materials generated electrical charge (polarization) upon mechanical stress [1]. The following year, the converse effect was discovered by Gabriel Lippmann through the mathematical aspect of the theory; an imposed voltage which yields a mechanical deformation of the material [1]. This unusual phenomenon was first studied in Rochelle salt and other single-crystal materials, such as quartz and tourmaline [1]. The technological breakthrough for piezoelectric materials came in the 1940s, when piezoelectricity and ferroelectricity were discovered in polycrystalline ceramic materials (or piezoceramics). Currently, applications and devices based on piezoelectricity are used in a large number of electronic equipments. [1, 2, 3].

Lead zirconate titanium, $PbZr_xTi_{1-x}O_3$ (PZT), is currently the most frequently used material for piezoelectric applications as it possesses exceptional dielectric and piezoelectric properties. Unfortunately, the material system contains high levels of lead which is toxic. The European Union (EU) included PZT in its directive *Restriction of the use of certain Hazardios Substances in electrical and electronic equipment (RoHS)* with the goal of replacing lead-based piezoelectric materials with safer options [4]. However, exceptions have been made for lead-containing piezoceramics due to the lack of suitable alternatives [3].

In recent years, environmental concers have strongly driven the need to replace lead-containing piezoceramics, creating a resurgence within the research field. Bismuth-based materials represent one class of potential candidates that have been suggested to replace the lead-based piezoceramics. Among these materials, bismuth potassium titanate, $Bi_{0.5}K_{0.5}O_3$ (BKT), has been widely studied and is a

well-known ferroelectric material with perovskite structure (ABO_3) of tetragonal symmetry at room temperature [5]. BKT exhibits promising polarization and strain performance as well as possessing a high operating temperature at about 380 ° C. The material is also an important component in solid solution systems that possess a morhoptropic phase boundary (MPB) similar to the one observed in PZT [3]. Solid solution systems such as (1-x)$Bi_{0.5}K_{0.5}TiO_3$-$x$$BiFeO_3$ (BKT-BFO) and (1-x)$Bi_{0.5}K_{0.5}TiO_3$-$x$$Bi_{0.5}Na_{0.5}O_3$ (BKT-BNT) have been investigated, among many material systems with encouraging results [6, 3].

BKT is regarded as a challenging material to fabricate with the conventional solid state synthesis. The preparation of the material often faces problems with densification and phase purity. These complications might be accredited to the volatility of potassium/bismuth oxides at elevated temperatures, yielding A cations and oxygen vacancies [5, 7]. Copper additives have successfully been used to increase the densification and piezoelectric properties of other piezoelectrics [8, 9, 10]. A recent published article [11] on BKT-BFO suggested that the addition of CuO compensated the A cation vacancies in the material, and further increased the piezoelectric performance of the material system.

1.2 Aim of work

The objective of this Masters thesis is to investigate the A to B stoichiometry, phase purity, density, as well as dielectric and piezoelectric properties of copper oxide (CuO) doped BKT. All materials will be prepared by the solid state synthesis. The first part of the study includes the investigation of BKT with excess bismuth and potassium. Crystal structure, sinterability, particle and surface morphology will be characterized using X-ray diffraction (XRD), Archimedes' method, and scanning electron microscopy (SEM), respectvely. The second part of the study includes the investigation of BKT with CuO addition. Crystal structure, sinterability, particle and surface morphology, as well as dielectric and piezoelectric properties will be analyzed.

Chapter 2

Literature review

2.1 Piezoelectricity and ferroelectricity

2.1.1 Piezolectricity

The word *piezo* originates from Greek, which means *to press*. The piezoelectric effect is a phenomenon that occurs when a crystal acquire an electric charge in response to an applied mechanical stress. The applied force generates a net movement of the positive and negative ions relative to each other, producing a polarization in the crystal, as illustrated in Figure 2.1. The conversion where the mechanical energy are transformed into electrical energy is called the direct piezoelectric effect [1]. Vice versa, the converse piezoelectric effect is the reverse process and occurs when a voltage is applied in the same direction as the polarization, and consequently results in a mechanical deformation (strain) of the crystal system [1]. For the direct piezoelectric effect, polarization is linear with respect to pressure. The reverse effect is, on the other hand, weaker and quadratic dependent [1].

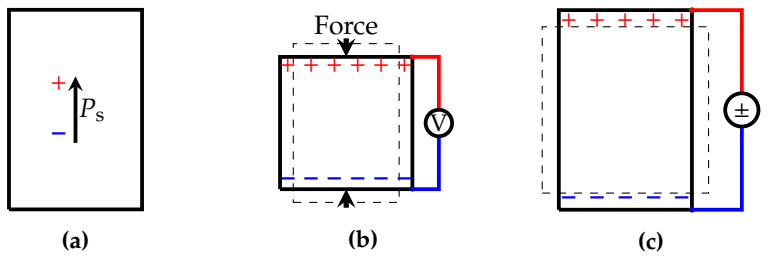

Figure 2.1: Schematic illustration of the piezoelectric effect: (a) Material with spontaneous polarization, P_s, at its original state; (b) direct piezoelectric effect, where a net polarization develops as a consequence of an applied mechanical stress; (c) converse piezoelectric effect, where the material expands as a response to an applied voltage [2].

2.2 Piezoelectric ceramics

2.2.1 Perovskite structure

Today, the most versatile and technologically common materials used for piezoelectric applications have the perovskite structure [1, 2, 3]. The name perovskite originates from $CaTiO_3$, and is now a general term for oxides with chemical composition ABO_3 [12]. The ideal perovskite structure has a space group[1] designation of $Pm\bar{3}m$. This ideal structure may be described as a simple cubic unit cell with a big 12-fold coordinated cation on each corner position (A-site), a smaller 6-fold coordinated cation in the center (B-site), and three oxygen anions on the face centered positions of the cubic cell. The structure is built up by a network of corner-linked oxygen octahedra with the smaller B cation filling the octahedral holes (BO_6), and the biggest A cation positioned at the dodecahedral holes. An illustration of the simple cubic structure is presented in Figure 2.2a [1, 3]. Oxygen anions are always in the form of O^{2-}, giving a net charge of -6. The cations must then have a net charge of +6, normally distributed as A^{+}/B^{5+}, A^{2+}/B^{4+}, or A^{3+}/B^{3+}.

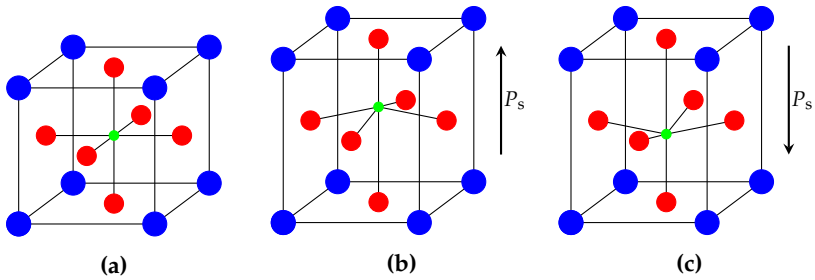

Figure 2.2: Schematic illustrations of the perovskite structure; (a) cubic structure with no polarization; (b) tetragonally distorted structure with polarization up; (c) tetragonally distorted structure with polarization down. Blue A cations occupies corner positions; green B cations occupies body center; while red oxygen atoms are situated at the face centers.

[1] A space group is a notation set used to describe the symmetry elements of a structure.

As explained above, the ideal perovskite structure is cubic. However, the relationship between the atomic size of the A and B cations does not always allow this crystal symmetry. To compensate, various distortions and tilting mechanisms of the unit cell occur in order to gain stabilization. In 1926, Goldschmidt [13] published an article that demonstrated the stability and distortion of the perovskite structure based on geometrical considerations. Using an ionic radii model, Goldschmidt proposed a simple concept known as the Goldschmidt's tolerance factor, t, which is expressed in equation 2.1:

$$t = \frac{r_A + r_O}{\sqrt{2}(r_B + r_O)} \tag{2.1}$$

where r_A, r_B and r_O are the ionic radii of the respective ions. It was estimated that the stability of the perovskite structure range from about $t = 0.77$ to $t = 1.05$, where the perfect cubic perovskite is formed at $t = 1$ [14]. For $t > 1$, the size of the B cation is too small to fit in the B-site. This is accompanied with a positional shift of the respective B-cation towards one of the oxygen anions. As a consequence, a tetragonal structure with polarization along the cubic (100) direction is typically formed in the range of $1 < t < 1.065$. Note that the polarization might point in both directions of the (100) direction, as illustrated in Figure 2.2b and 2.2c [3]. At larger values of t, the perovskite structure becomes unstable and the more stable hexagonal structure is developed instead. For $t < 1$, the A cation is too small to fit in the A-site, which result in a rhombohedral structure. At even smaller values of t, the crystal changes from a rhombohedral to an orthorombic crystal structure [2].

Today, the most well-known piezoelectric perovskites are $BaTiO_3$, $PbTiO_3$, and $KNbO_3$. In addition to these single-components, various solid solution systems containing different piezoelectric perovskites have been investigated with interesting dielectric and piezoelectric results [15]. For instance, a solid solution of $PbZrO_3$ and $PbTiO_3$ (PZT) is by far the the greatest piezoelectric material on the market today [1, 16].

The piezoelectric solid solution material systems are often prepared with the objective of imposing a morphotropic phase boundary (MPB), which refer to the phase transition that occurs as a response to the change in composition. In

piezoelectric sense, this applies to the phase transition between the tetragonal and the rhombohedral ferroelectric phases [1]. Properties such as piezoelectric coefficient[2], dielectric permittivity and electromechanical coupling factor[3] are maximized in solid solutions of perovskite-type piezoelectrics at compositions close to the MPB [3].

2.2.2 Crystallographic sub-groups

Piezoelectricity can be predicted from the symmetry of crystal point groups [1]. There are thirty-two different crystallographic point group symmetries. Eleven posses a center of symmetry and are non-polar [1]. An applied stress to these crystals result in symmetrical ionic displacement, and therefore gives no net change in dipole moment. The other twenty-one are non-centrosymmetric, and all besides one of these are piezoelectric crystals. The single exception contains symmetry elements that cancel each other out when a mechanical force is introduced [1]. Among the twenty piezoelectric classes, ten are pyroelectric [1]. These crystals have a *unique* polar axis and possess the unusual feature of being permanently polarized within a given temperature region. In other words, the dipole moment is integrated in the structure regardless of any imposed electric field or mechanical stress [1, 2].

Among the pyroelectric crystals, some have reorientable polarization. These crystals possess a spontaneous polarization that can be reversed by applying an external electric field [1]. Materials with this behavior are called ferroelectric materials (or ferroelectrics). In ferroelectrics, a structural phase transformation from a low-temperature ferroelectric phase to a high-temperature non-ferroelectric (or paraelectric) phase occurs at the Curie temperature, T_c. Unlike the ferroelectric behavior, no polarization is retained in paraelectric crystals in the absence of an electric field.

Note that pyroelectricity is a fundamental phenomenon that is slightly different

[2]Piezoelectric coefficient is the polarization generated per unit of mechanical stress applied to a piezoelectric material. Alternatively, the mechanical strain experienced by a piezoelectric material per unit of electric field applied.

[3]Electromechanical coupling factor is an indicator of the effectiveness which a piezoelectric material converts electrical energy into mechanical energy, and vice versa.

in nature from piezoelectricity as it rests on other symmetry conditions. Conventionally, all pyroelectrics are piezoelectrics, but not all piezoelectrics are ferroelectrics. Similarly, ferroelectricity is a distinction from one type of pyroelectricity and can be separated through experimental observations [1, 17]. A descriptive schematic of the various piezoelectric classes are shown in Figure 2.3.

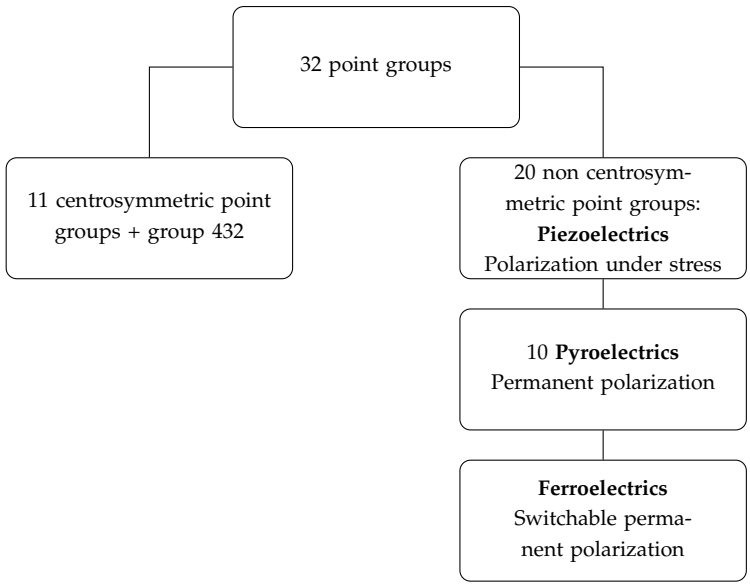

Figure 2.3: Point group requirements for piezoelectric, pyroelectric and ferroelectric ceramics.

2.2.3 Ferroelectric domains and poling

The ferroelectric breakthrough came in the 1940s with the discovery of the perovskite $BaTiO_3$. It was then observed that an external electric field could orient the spontaneous polarization in the material. In the years after this breakthrough, research into polycrystalline piezoelectric ceramics bloomed [2].

The spontaneous polarization in a piezoelectric crystal is normally not uniformly aligned along the same direction throughout the whole crystal. However, small areas within the crystal can have uniformly oriented spontaneous polarization.

These uniformly polarized regions are called ferroelectric domains. The domains are separated by interfaces called domain walls. These domain walls distinguish neighboring areas of different uniform polarization direction, as sketched in Figure 2.4a [18]. When a ferroelectric material is cooled through the paraelectric-ferroelectric phase transition, domain structures are formed in order to minimize the sum of elastic, electrostatic, domain wall, and surface energy in each grain [18].

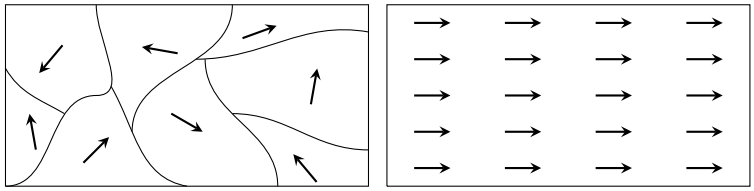

(a) No applied electric field. **(b)** With applied electric field.

Figure 2.4: Sketch of the domains with the corresponding polarization direction: (a) Unpoled ferroelectric material with zero net polarization; (b) poled ferroelectric material with nonzero net polarization.

In ferroelectrics, all the randomly oriented domains within a crystal can be aligned in the same direction by an external electric field, as shown in Figure 2.4b. This process is referred to as *poling*. The most important characteristic of ferroelectrics is the ferroelectric hysteresis loop (P-E loop), which is observed through polarization reversal by an electric field, illustrated in Figure 2.5 [1]. At low electric field levels, the polarization increases linearly as a function of the field strength. This corresponds to the AB segment in Figure 2.5. Here, the small value of the electric field cannot switch the domains with unfavorable directions of polarization. However, as the field increases, more of these domains begin to switch in the direction of the field. A rapid increase of polarization is observed in segment BC, wheras all domains become aligned at point C. A saturated polarization is therefore achieved in segment CD. Once the field strength starts to decrease, the domains will back-switch, consequently decreasing the polarization. At zero field strength, some domains would still retain their alignments and the polarization is nonzero. Here, the residual polarization in point E is called *remnant polarization*, P_{r}. The net polarization reaches zero if the electric field is further

reversed, which is shown in point F. This point is commonly referred to as the negative *coercive field*, E_c. A new saturation point in the opposite direction, is reached in point G if the electric field is sufficiently increased in negative direction.

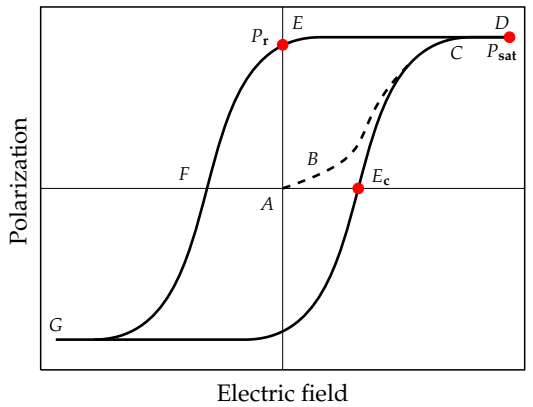

Figure 2.5: Ferroelectric polarization-electric field hysteresis loop. P_{sat} is the saturation polarization; P_r is the remnant polarization; and E_c is the coercive field, marked with red dots. $A - G$ segment corresponds to one cycle of poling.

2.2.4 Relaxor ferroelectrics

Relaxor ferroelectics (or relaxors) are a class of disordered crystals possessing peculiar structure and properties. They are a subgroup of ferroelectrics and possess extraordinary dielectric properties. Cross [19] published an article in 1987 that distinguished relaxors from normal ferroelectrics crystals by three distinct characteristics. First, in the dielectric response, relaxors exhibit a large and broaden peak (ϵ'_{max}) in the temperature dependency of relative dielectric permittivity, as shown in Figure 2.6. Another distinct feature is that the peak temperature (T_m) of ϵ'_{max} decreases with decreasing frequency [19]. Second, when relaxors are exposed to an electric field, they have the same behavior as normal ferroelectrics at low temperature regions. However, the P-E hysteresis loop slowly degenerates towards nonlinearity as the temperature increases, as shown in Figure 2.7. This behavior implies that the phase transition from paraelectric to long-range-ordered ferroelectric state does not corresponds to an abrupt transition as seen

in normal ferroelectrics [20, 21]. Third, no macroscopic phase change is observed for relaxors with optical and x-ray radiation below the Curie temperature [19].

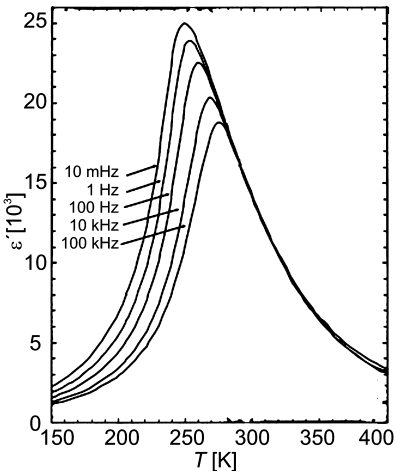

Figure 2.6: Dielectric response of relaxors. The temperature dependency of the relative dielectric permitivitty measured with difference frequencies for a single-crystal $Pb(Mg_{1/3}Nb_{2/3})O_3$ by Bokov et al. [20].

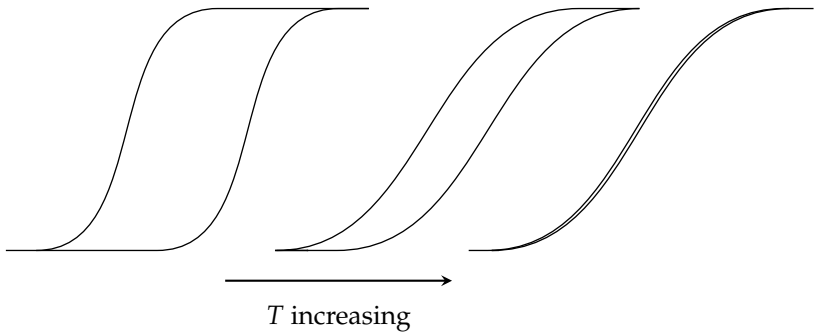

Figure 2.7: The hysteresis response in relaxor ferroelectrics. The hysteresis loop slowly degenerate with increasing temperature. Temperature is denoted as T.

The unusual characteristics of relaxor ferroelectrics are closely related to the ap-

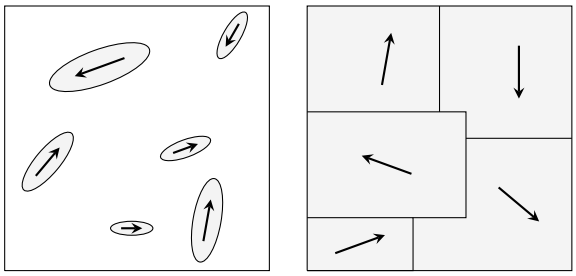

Figure 2.8: Schematic representation of the two PNR models in relaxors suggested by Bokov et al. [20]; (a) local "phase transitions" or phase fluctuations that is embedded into a cubic matrix, where the structural phase remains unchanged; (b) PNRs occurs throughout the crystal, where the crystal consist of low-symmetry nanodomains separated by the domain walls but not by the regions of cubic symmetry. Grey area represents polar nanoregions, while white corresponds to region of cubic symmetry.

pearance of *polar nanometer regions* (PNR) [20]. At elevated temperatures relaxors exist in a non-polar paraelectric phase, much similar to the paraelectric phase of normal ferroelectrics. Upon cooling, randomly distributed nanoregions with dipole moments arise. The appearance of these dipole moments occurs at the transition temperature (Burns temperature). The transition at the Burns temperature, which is far above T_{m}, is not believed to be a structural phase transition as no change in crystal structure on a macroscale is observed [20, 21]. Bokov et al. [20] explained the formation of PNRs by subdividing them into two categories, as sketched in Figure 2.8: (a) PNRs is a result of local "phase transitions" or phase fluctuations that is embedded into a cubic matrix, where the structural phase remains unchanged; (b) the apperance of PNRs occurs throughout the crystal, where the crystal consist of low-symmetry nanodomains separated by the domain walls but not by the regions of cubic symmetry.

The large and relatively high-temperature-stable dielectric permittivity makes relaxors a good candidate for capacitor applications. Systems based on KNN ($K_{0.5}Na_{0.5}NbO_3$) and BNT can exhibit permittivity values above 2000 with variation ($\frac{\Delta\epsilon}{\epsilon_0}$) less than 10 % in a temperature range of about 200° C [21].

2.2.5 Lead zirconium titanate

Lead zirconium titanate ($PbZr_{1-x}Ti_xO_3$) is the most commonly used material for transducer applications [2]. The material is suitable for various applications due to several desirable and tunable properties. PZT is often used with composition close to the morphotropic phase boundary ($x = 0.48$) where properties such as piezoelectric coefficient, dielectric permittivity and electromechanical coupling factor are maximized [3].

One way of optimizing PZT for various applications is to use PZT with additives. A large amount of research has been carried out on lead lanthanum zirconate titanate materials (PLZT). The high solubility of lanthanum in the basic PZT system makes it possible to tailor specific chemical compositions with various combination of desired properties. This include chemical compositions from those best suited for dielectric and piezoelectric applications to those specifically tailored for electrooptic performance [2]. The electrooptic properties and the high optical transparency makes the material well suited for applications such as light shutters, coherent modulators, color filters, segmented displays and image storage devices [2].

2.2.6 Technological perspective

The applications of piezoelectric ceramics are diverse, covering all areas of our everyday life. Their simplicity, adaptibility, compact size, low cost, and high reliability have made these materials very attractive among design engineers, finding them in an increasing number of applications [2]. One class of applications for piezoelectric ceramics are that of transducers, which are devices that convert one energy form into another form of energy. The direct piezoelectric effect is utilized to convert mechanical energy into electrical signals. Some examples of typical devices that use this effect is microphones, gas igniters, and accelerometers [22]. Oppositely, the converse piezoelectric effect are used in devices such as pumps, loud speakers, and actuators [22].

Another class of application for piezoelectric ceramics are that of capacitors. The first discovered ferroelectric ceramic, $BaTiO_3$, was first used as a ceramic capac-

itor, before the discovery of the ferroelectric nature of the material. The high dielectric constant observed in piezoelectric ceramics makes them suitable for high-dielectric-constant capacitors [2].

2.3 Point defect chemistry

2.3.1 Point defect

The perfect crystal can be achieved, hypothetically, only at 0 K; at finite temperatures crystals are imperfect. An imperfect crystal may contain various type of defects. The fact that real materials are not perfect crystals is critical to materials engineering. If materials were perfect crystals, properties would be restricted to their crystal structure and composition alone. However, the possibility of making imperfect crystalline materials creates the opportunity of manipulating material properties into combinations that modern engineering requires.

Point defects are disturbances of the crystal pattern at an isolated site. There are two categories of point defects: intrinsic and extrinsic defects. An intrinsic defect is formed when an atom is missing from a lattice position that was originally filled in the crystal. This atom can either be totally removed from the crystal, or occupy an interstitial site where no atoms originally appear. Extrinsic defects refer to foreign atoms that are introduced to the material. Dopants are intentionally added to the material, while impurities occurs unintentionally. [23].

The development of oxygen vacancies stabilizes the domain pattern and limits the domain wall movement due to the formation of pinning centers. Pinning centers is belived to be physical defects, for instance a pair of point defects (e.g. $Fe'_{Zr,Ti} - V_O^{\bullet\bullet}$). Three models have been proposed to describe this phenomenon [24]; (1) the bulk effect (charged defects that aligns parallel with the polarization within a domain); (2) the domain wall effect (charged defects that diffuse towards domain walls creating pinning centers); (3) the interface effect (charged defects which moves towards the grain boundaries).

2.3.2 Kröger-Vink notation

Kröger-Vink notation is a modified notation set used to describe point defects in chemical reactions [25]. The nomenclature for the species are made up by three parts; the body, the subscript and the superscript. The following equations describes intrinsic point defects with Kröger-Vink notation:

$$Na^{x}_{Na} + Cl^{x}_{Cl} \rightarrow V^{'}_{Na} + V^{\bullet}_{Cl} + NaCl \tag{2.2}$$

$$Ag^{x}_{Ag} \rightarrow V^{'}_{Ag} + Ag^{\bullet}_{i} \tag{2.3}$$

Here, equation 2.2 and 2.3 describes the Schottky and Frenkel defect, respectively. The body represents the species involved, a chemical symbol of an element, or the letter V for vacancy. The subscript represents the crystallographic position occupied by the original species involved, either a lattice or an interstitial site denoted as *i*. The superscript describes the effective electric charge of the site with respect to a perfect crystal. Each positive charge is denoted as $^{\bullet}$, each negative charge as $'$, and neutral charge as ^{x} [25]. In addition to the normal rules for balancing chemical equations, the number of original lattice sites on both side of the equation must be preserved [25]. It is worth mentioning that vacancies and interstitial sites do not influence the balance rule, since vacancies are not mass and interstitials are not a part of the ideal crystal. A schematic illustration of Schottky and Frenkel defects is shown in Figure 2.9.

2.3.3 Extrinsic point defects

Extrinsic point defects are foreign atoms which are introduced to the material. These defects can have a large effect on engineering properties, and are particulary used to tailor electrical and mechanical properties. As described in Section 2.2.5, PZT is nearly always used with some kind of dopant, depending on the desired properties. There are three different types of substitution that might occur when adding additives to PZT [2]:
Isovalent:

$$SrO + ZrO_2 \xrightarrow{PZT} Sr^{x}_{Pb} + Zr^{x}_{Zr/Ti} + 3O^{x}_{O} \tag{2.4}$$

Here, Sr^{2+} replaces isovalent Pb^{2+}. Isovalent doping of PZT may cause effects

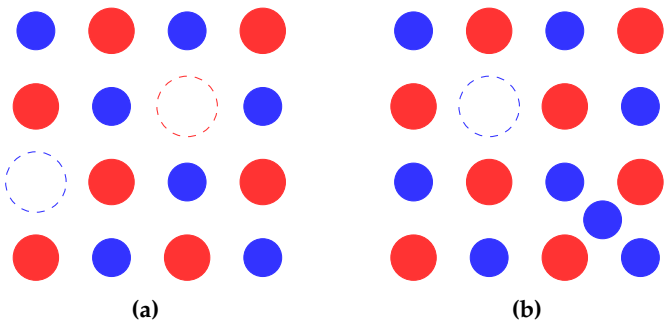

Figure 2.9: Schematic illustration of the intrinsic defects; (a) Schottky defect; (b) Frenkel defect. Cations are marked as blue, while anions are marked as red.

such as inhibited domain orientation, higher aging rates and poorly developed hysteresis loop [2]. Note that the notation in equation 2.4 indicates that the compounds on the left hand side of the arrow are introduced to the material which is noted above the arrow [25].
Donor doping:

$$La_2O_3 + ZrO_2 \xrightarrow{PZT} 2La^{\bullet}_{Pb} + Zr^{x}_{Zr/Ti} + 5O^{x}_{O} + V''_{Pb} \tag{2.5}$$

Here, La^{3+} replaces Pb^{2+} to create an extra charge on the A-site. PZT is often donor doped to counteract the natural p-type conductivity arising from oxygen vacancies in the material. This can subsequently increase the electric resistivity of the material by at least three orders of magnitude. The effect of donor doped ceramics are usually characterized by square hysteresis loop, low coercive fields, high remnant polarization, high dielectric loss and reduced aging [2].
Acceptor doping:

$$Fe_2O_3 + 2PbO \xrightarrow{PZT} 2Fe'_{Zr/Ti} + 2Pb^{x}_{Pb} + 5O^{x}_{O} + V^{\bullet\bullet}_{O} \tag{2.6}$$

Here, Fe^{3+} replaces Ti^{4+} to create a extra hole on the B-site. The extra holes is compensated by creating oxygen vacancies. The effect of these additives are characterized by poorly developed hysteresis loop, lower dielectric constant and higher aging rates [2].

2.3.4 Defect symmetry principle

The bulk effect might be described with the defect symmetry principle, which explains the relationship between crystal symmetry and the symmetry of statistical short-range order distribution of point defects. The simple perovskite structure of $BaTiO_3$ doped with Mn^{3+} ions will be used as an example to explain this principle, as described in Ren et al. [26]. Mn^{3+} ions will occupy the Ti^{4+} position (B-site) due to similarities in ionic radius [26]. As a result, O^{2-} vacancies are created due to charge neutrality:

$$Mn_2O_3 + BaO_2 \xrightarrow{BaTiO_3} Ba_{Ba}^{x} + 2Mn_{Ti}^{'} + 5O_{O}^{x} + V_{O}^{\bullet\bullet} \tag{2.7}$$

Accordingly, Mn^{3+} dopants and O^{2-} vacancies are the corresponding point defects in this material system. Point defects are thought to be distributed randomly within the $BaTiO_3$ host crystal. However, if we consider the local environment surrounding a given defect, the short-range distribution of other defects around it may show some kind of statistical symmetry, i.e. the short-range distribution of the O^{2-} vacancies surrounding a given Mn^{3+} dopant in Mn-doped $BaTiO_3$ [26]. This statistical distribution is refered to as defect symmetry. The defect symmetry principle may be explained in two different ways, as $BaTiO_3$ has different crystal symmetry in the paraelectric and ferroelectric state.

In the paraelectric state ($T > T_c$), the material has cubic symmetry. Here, the distance from the Mn^{3+} dopant (B-site) to the surrounding six O^{2-} sites are equivalent. The defect probability should therefore be equal for all six O^{2-} sites, as illustrated in Figure 2.10a. In other words, the point defects have cubic defect symmetry at equilibrium [26].

The material transforms into ferroelectric state when cooled below T_c. As was previously stated, a spontaneous polarization is developed along the (001) directions due to the relative displacement of positive and negative ions. This yields a polarized tetragonal crystal. This phase transformation is diffusionless, implying that point defects cannot migrate [26]. Therefore, the point defect distribution will remain the same as in the paraelectric state, which means that the cubic defect symmetry remains unchanged straight after the phase transforma-

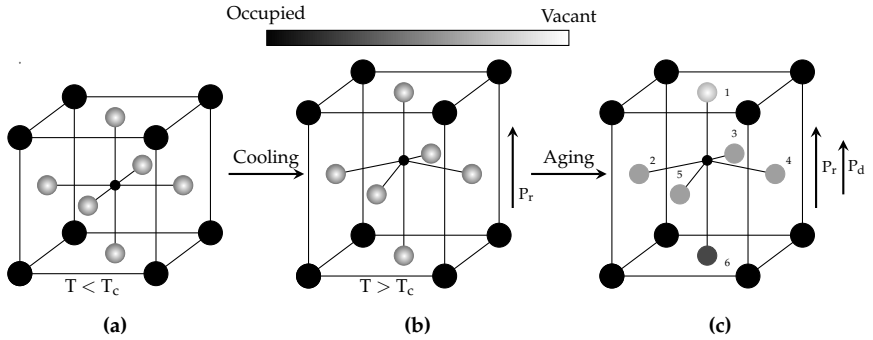

Figure 2.10: Defect symmetry and the related crystal symmetry of Mn-doped $BaTiO_3$ (Mn^{3+} at Ti^{4+} sites). (a) Paraelectric state at equilibrium; (b) immediately after paraelectric-ferroelectric phase transition at T_c; (c) ferroelectric state at equilibrium (after aging). The color gradient represents the probability of finding an O^{2-} vacancy at O^{2-} site. Long arrow refers to the spontaneous polarization P_s, and short arrow refers to the defect polarization P_d. T_c is the paraelectric-ferroelectric phase transition temperature [26].

tion, as shown in Figure 2.10b. However, such state is not very stable. Geometrical considerations indicate that the distance between the six O^{2-} anions to the Mn^{3+} cation at the B-site are not equivalent. It is therefore natural to assume that the closest site have largest defect probability due to the Coulomb attractive force between the effectively negative Mn^{3+} dopant and the effectively positive charge O^{2-} vacancy. Yielding a short-range migration of O^{2-} vacancy to site 1 from the other oxygen sites (site 2, 3, 4, 5, and 6) as shown in Figure 2.10c. This *aging* process needs some time to complete. When equilibrium is reached, the defect dipoles can align with the polarization direction within a domain.

If an electric field is applied to an aged crystal, the spontaneous polarization can be changed instantaneously. However, the defect symmetry and the corresponding P_d will remain unchanged. The removal of the electric field will therefore cause a reversible domain switching due to the unchanged defect symmetry and the corresponding P_d. Consequently, developing a pinched P-E hysteresis loop, as described in 2.11.

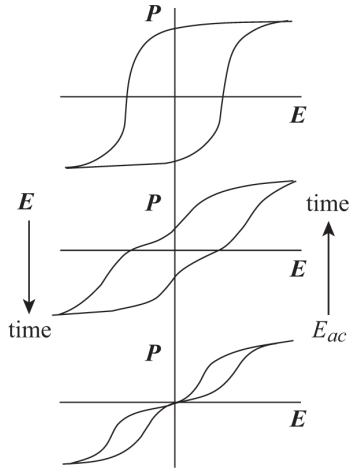

Figure 2.11: The evolution of polarization-electric field (P-E) hysteresis loops as a consequence of pinning centers with respect to time by Jonker [27]. Pinched P-E loop is caused by pinning centers.

2.4 Bismuth potassium titanate

2.4.1 Overview of BKT

Bismuth-based materials have received attention as possible alternatives to lead-free piezoelecric materials due to their piezoelectric properties and non-toxicity. Piezoelectric ceramics such as BKT, BNT, and BFO has been widely studied with promising results [3].

BKT was first synthesized in 1957, however, its ferroelectricity was uncovered in 1962 by Buhrer [28]. The ceramic is a tetragonally distorted relaxor ferroelectric perovskite with high depolarization and Curie temperature at about 270° C and 380° C, respectively [3, 29]. The properties of pure BKT ($\epsilon_r = 769$, d_{33} = 82 - 101 pC/N, $S_{\max}/E_{\max} \sim 133$ pm/V [5]) are regarded as promising, but not excellent when compared with PZT ($\epsilon_r \sim 2300$, d_{33} = 410 pC/N, , $S_{\max}/E_{\max} \sim 700$ pm/V [30]). However, since the room temperature tetragonal crystal structure is only limited to a few compositions (i.e., $BaTiO_3$ and $PbTiO_3$), BKT has proven itself as

an important end-member of solid solutions for lead-free piezoelectric materials [6, 31, 32].

2.4.2 Structure and properties

The perovskite structure of BKT consists of Bi^{3+} and K^{+} ions located on the corners filling the dodecahedral holes, Ti^{4+} ions distorted from the body center in the oxygen octahedra, and O^{2-} ions located in the centers of the faces. The ferroelectric nature of BKT occurs due to the displacement of the Ti^{4+} ions, which creates a polar crystal with spontaneous polarization parallel to the c-axis. The ferroelecric BKT structure is shown in Figure 2.12.

Upon heating, the material undergoes a second-order phase transition from tetragonal to pseudocubic phase at about 270° C [29]. A ferroelectric breakdown occurs at about 380° C, as the material transforms into a cubic phase, i.e., the ferroelectric-paraelectric phase transition. Figure 2.13 presents the lattice parameters, a and c, plotted against temperature, determined by Ivanova et al. [29].

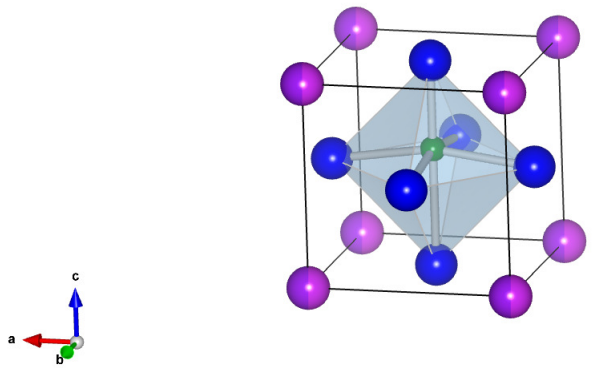

Figure 2.12: BKT structure at room temperature; Bi^{3+} (dark purple) and K^{1+} (light purple) in the corners; Ti^{4+} (green) distorted from the body center; and O^{2-} (blue) at the center of the faces. The structure are made by the visualization tool Vesta [33].

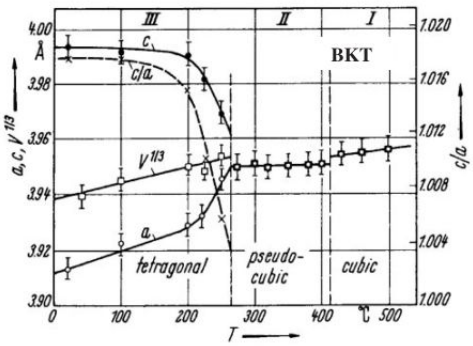

Figure 2.13: Phase diagram of $Bi_{0.5}K_{0.5}TiO_3$ with respect to lattice parameter and temperature by Ivanova et al. [29]. The tetragonal-pseudocubic phase transition occurs at about 270° C, while the pseudocubic-cubic phase transition occurs at about 380° C.

2.4.3 Synthesis

BKT has proven to be challenging to prepare due to problems with densification and phase purity [5, 7]. König et al. [7] has suggested that these problems might be related to the volatility of A-site cations at high sintering temperature. The evaporation of Bi_2O_3/K_2O will lead to A cation and oxygen vacancies, as described in equation 2.8 and 2.9:

$$2K_K^x + O_O^x \rightarrow 2V_K^{'} + V_O^{\bullet\bullet} + K_2O(g) \tag{2.8}$$

$$2Bi_{Bi}^x + 3O_O^x \rightarrow 2V_{Bi}^{'''} + 3V_O^{\bullet\bullet} + Bi_2O_3(g) \tag{2.9}$$

It is believed that the perovskite structure can only accommodate a certain level of vacancies. If this solubility level is exceeded, secondary phases might be develop. The formation of $K_2Ti_6O_{13}$ and $K_4Ti_3O_8$ are often pointed out as a problem [5, 34, 7]. The ratio of bismuth and potassium evaporation has, on the other hand, not been given much attention in studies. As for titanium, B-site vacancies are not considered to form in the BKT structure.

The conventional solid state synthesis has earlier been suggested as a difficult way of preparing BKT [5]. However, Wefring et al. [31] recently reported the preparation of phase pure BKT ceramics with a relative density of 97 % using this method.

2.4.4 CuO doping

Copper additives have successfully been used to increase the densification and piezoelectric properties of other piezoelectrics [8, 9, 10]. A recent published article [11] on BKT-BFO suggested that the addition of CuO compensated the A cation vacancies in the material, and further increased the piezoelectric performance of the material system.

The introduction of CuO to the BKT perovskite structure yields three possible types of substitution: (1) the Cu^{2+} ions substitute for K^{+} ions on A-site; (2) the Cu^{2+} ions substitute for Bi^{3+} ions on A-site; (3) or the Cu^{2+} ions substitute for Ti^{4+} ions on B-site. Equation 2.10 - 2.11 describe the mentioned substitution options:

$$CuO \xrightarrow{BKT} Cu_K^{\bullet} + V_K^{'} + O_O^{x} \tag{2.10}$$

$$2CuO \xrightarrow{BKT} 2Cu_{Bi}^{'} + V_O^{\bullet\bullet} + 2O_O^{x} \tag{2.11}$$

$$CuO \xrightarrow{BKT} Cu_{Ti}^{''} + V_O^{\bullet\bullet} + O_O^{x} \tag{2.12}$$

Note that Cu^{2+} acts as a donor in option (1), while it acts as an acceptor for option (2) and (3). As described above, it is believed that the nominal stoichimetric samples of BKT are in reality A deficient, due to evaporatation of A-cations. This implies that the expected A:B 1:1 stoichimetry is more likely shifted towards a B-rich region. In that case, two more options must be taken into consideration, as the addition of CuO might incorporate into vacant A and oxygen sites. Equation 2.13 and 2.14 describe the relevant mechansism

$$CuO + V_K^{'} + V_O^{\bullet\bullet} \xrightarrow{BKT} Cu_K^{\bullet} + O_O^{x} \tag{2.13}$$

$$CuO + V_{Bi}^{'''} + V_{O}^{\bullet\bullet} \xrightarrow{BKT} Cu_{Bi}^{'} + O_{O}^{x} \tag{2.14}$$

for CuO occupying vacant A and oxygen sites, respectively. In both cases, the concentration of A-cation and oxygen vacancies are reduced. As described in Section 2.3, the reduction of oxygen vacancies would reduce the pinning effect. This will generally enhance the domain wall motion, and increase the piezoelectric properties of the material.

2.5 Solid state synthesis

In this work, BKT was prepared by the conventional solid state synthesis. The method involves mixing and heating of two or more non-volatile compounds at a temperature below their melting temperatures. The desired product is achieved by reaction between the reactants. However, the reaction is relatively slow. Therefore, a high temperature ($T > 500^{\circ}$ C) is often required, as the diffusion rates of the reactants increases with respect to temperature [35]. Large separations between reactants make it harder for a complete solid state reaction throughout the precursor sample. This means that the reactant mixture must be well-mixed and grounded into small particles to induce the reactivity.

Calcination refers to a high-temperature treatment of a powder mixture to modify the characteristics of the powder. The modifications that are achieved by calcining is coarsening, decomposition, dehydration and reaction [35]. Calcining is also performed to prevent build up of gases that can cause cracks during consolidation [35].

The calcined powder is compacted into the desired shape by pressure. Uniaxial pressing are performed by consolidating powder in a die with pressure along one single axial direction. Cheap and high production rate is achieved with this procedure. However, problems such as density variation and cracking may arise [35]. The limitations of unixial pressing can be overcome by isostatic pressing, as pressure is applied from all directions. The relative density obtained by isostatic pressure is usually higher and more uniform compared to uniaxial pressing [35].

Sintering is the densification process of the ceramic. This procedure is normally conducted just below the melting temperature, and the aim is to remove pores between particles [35]. The dominant mechanisms for transport are diffusion and viscous flow. Heat is the primary source of energy, used to induce the the growth and bonding between neigboring particles. The sintering process can be divided into three stages. The intial stage involves rearrangement and initial neck formation between adjacent particles. Following, the intermediate stage is where most of the densification occurs. Here, the particles moves closer together and the neck growth increases. Some particles will grow at the expense of others, depending on the curvature of the grain boundary [35]. The final stage involves the final removal of porosity which is removed by vacancy diffusion along grain boundaries [35]. The removal of porosity and vacancy diffusion are dependent on controlled grain boundary movement and grain growth as fast growth may isolate pores inside the grains. Isolated pores are harder to eliminate [35].

Chapter 3

Experimental Work

3.1 Sample composition

The aim for this experimental work was to prepare and characterize modified samples of BKT, listed in Table 3.1 with composition and abbreviatons used throughout this text.

Table 3.1: Composition and abbreviation of the modified samples of BKT.

Sample composition	Abbreviation
$Bi_{0.5}K_{0.5}TiO_3$	BKT-0
$Bi_{0.5}K_{0.5}TiO_3$ + 1 mol% (Bi + K)	BKT-1
$Bi_{0.5}K_{0.5}TiO_3$ + 2 mol% (Bi + K)	BKT-2
$Bi_{0.5}K_{0.5}TiO_3$ + 2 mol% (Bi + K) + 0.3 mol% CuO	BKTC-0.3
$Bi_{0.5}K_{0.5}TiO_3$ + 2 mol% (Bi + K) + 0.6 mol% CuO	BKTC-0.6
$Bi_{0.5}K_{0.5}TiO_3$ + 2 mol% (Bi + K) + 0.9 mol% CuO	BKTC-0.9

3.2 Synthesis

Preparation of calcined powder

Bismuth potassium titanate powder was prepared by the conventional solid state synthesis as reported by Wefring et al. [31]. Reagent-grade metal oxide powders of Bi_2O_3 (99.999 %), K_2O_3 (99.99 %) and TiO_2 (99.99 %) were used as precursors [31]. Stoichiometric amounts, listed in Table 3.2, were mixed according to the reaction described by equation 3.1:

$$Bi_2O_3 + K_2CO_3 + 4TiO_2 \rightarrow 4Bi_{0.5}K_{0.5}TiO_3 + CO_2 \tag{3.1}$$

Reactant powders were weighed before and after drying in a vacuum furnace (200° C, 10^{-2} mbar) overnight. Weight difference was assumed to be water, and the fraction of water in each precursor was calculated. The water content was then compensated with additional reactant powder according to the calculations, assuring that the desired amount of precursors were obtained.

Table 3.2: Mass of reactant powders.

Precursor	**Weight [g]**
Bi_2O_3	26.4864
TiO_2	18.1592
K_2O_3	7.8560

Following, stoichiometric amounts of precursors were crushed and mixed by wet ball-milling (24 h, 130 rpm) in isopropanol, using a 250 mL polyethylene (PE) bottle with 600 g of 5- mm yttrium-stabilized ZrO_2 balls. The amount of isopropanol were gradually added until the desired viscosity was achieved. The milling speed was adjusted to give approximately 60° milling ball angle.

After milling, the PE bottle and milling balls were rinsed with isopropanol, and the obtained slurry was dried under low pressure using a rotary evaporator (bath temperature = 43° C, 48 mbar). The dry precursor mixture was collected with a plastic spatula and crushed in a mortar. Then, the powder was calcined (720° C, holding time = 3 h, heating and cooling rate = 300° C/h) using an aluminia crucible with a lid to minimize the evaporation of A-site cations.

After calcination, the powder was once again milled (24 h, 130 rpm) with the same procedure as described above. Since larger particles was assumed to appear after calcination, less isopropanol was used. Once again, the PE bottle and milling balls were rinsed with isopropanol, and the obtained slurry was dried using a rotary evaporator (bath temperature = 43° C, 48 mbar). A second round of calcination was conducted, following the same procedure as already described. Afterwards, the powder was collected with a plastic spatula and dried overnight in an oven (110° C) to remove remaining moisture. Next,

the powder was crushed and grounded using a mortar and pistil, and sieved through a 250 μm mesh stainless steel sieve.

Addition of bismuth and potassium

Excess A cations were added to the calcined powder to compensate for potential loss of bismuth and potassium during calcination. The resulting calcined powder was therefore mixed with different amounts of bimuth(III)nitrate pentahydrate ($Bi(NO_3)_3{\cdot}5H_2O$) and potassium nitrate (KNO_3). This was conducted by first dissolving the mentioned compounds in distilled water, according to equations 3.2 and 3.3:

$$KNO_3(s) \rightarrow K^+(aq) + NO_3(aq) \tag{3.2}$$

$$Bi(NO_3)_3 \cdot 5H_2O(s) \rightarrow Bi^{3+} + 3NO_3 + 6H_2O(aq) \tag{3.3}$$

Next, the calcined powder was added to the different nitrate solutions, and dried in an oven (60° C) until all water had evaporated. The samples were then heat treated in an oven (400° C, holding time 3 h). Afterwards, the modified samples were sieved through a 250 μm mesh stainless steel sieve.

Addition of copper(II) oxide

Next, copper(II) oxide (CuO) was added to the calcined powder with 2 mol% of excess A cations (BKT-2). This was done by dividing the powder into several smaller samples and mixed with various amount of copper(II) nitrate ($Cu(NO_3)_2{\cdot}6H_2O$) as listed in Table 3.1. CuO was introduced to the samples by first dissolving $Cu(NO_3)_2{\cdot}6H_2O$ in distilled water according to equation 3.4:

$$Cu(NO_3)_2 \cdot 6H_2O(s) \rightarrow Cu^{2+}(aq) + 2NO_3(aq) + 6H_2O(aq) \tag{3.4}$$

Calcined powder was then added to the aqueous copper(II) nitrate solutions, and dried in an oven (70° C) until all water had evaporated. Next, the samples were again placed in an oven (400° C, holding time = 3 h) in order to CuO on the

particle surface of the BKT-2 powder, as shown in Figure 3.1. The formation of CuO is described by equation 3.5:

$$2Cu(NO_3)_2(s) \rightarrow 2CuO(s) + 4NO_2(g) + O_2(g) \tag{3.5}$$

To do (??)

Similar to previous section, the modified samples were sieved through a 250 μm mesh stainless steel sieve.

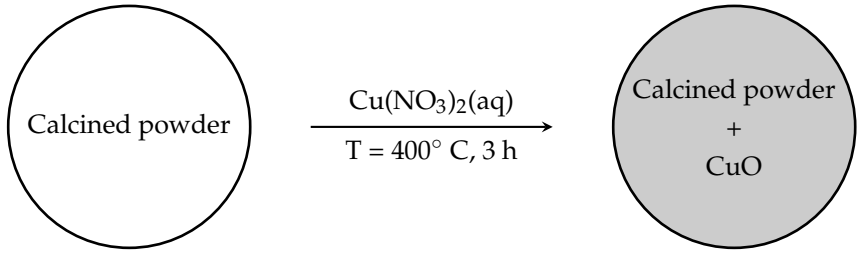

Figure 3.1: Schematic of calcined powder with CuO on its surface. A mixture of BKT and $Cu(NO_3)_2$ are heated at 400° C for 3 h. The grey color represent CuO.

Sintering pellets

Pellets were prepared from the samples, listed in Table 3.1. The powder samples were first pressed by an unixial press ($\sim$ 60 MPa, holding time = 2 min) using a stainless steel die. The resulting pellets were placed in several layers of latex condoms. The air inside was evacuated and the condoms were sealed. These samples were isostatically pressed by a cold isostatic press (2 kbar, holding time = 2 min).

After pressing, the pellets were placed in alumina crucibles, on a bed of sacrifical powder (unpressed calcined powder of BKT). Lids were located on top of the crucibles for the same reasons mentioned for calcination. The prepared samples were sintered (1060° C, holding time = 3 h, heating and cooling rate = 300° C/h) in unmodified atmosphere and pressure.

3.3 Characterization

The main characterization methods used in this thesis are X-ray diffraction (XRD), scanning electron microscope (SEM), energy dispersive X-ray spectroscopy (EDS), dielectric spectroscopy, piezoelectric analyzer, and Archimedes' method.

3.3.1 Structural characterization

The crystal structure of the different samples were studied using XRD (Siemens D5005 difractometer with CuK_α-radiation and secondary monochromator). Diffractograms were obtained from calcined and sintered samples. XRD samples of calcined powder were prepared by placing powder in single crystal silicon holders with a small cavity. As for the sintered pellets, crushed and uncrushed samples were measured. For crushed samples, the surface was grounded off, and the remaining mass were crushed and grounded using a mortar and pistil. The remaining powder was annealed (600° C, 1 h) in an alumina crucible to remove induced mechanical stress achieved during crushing. Likewise, crystal silicon holders with a small cavity were used for the crushed sintered pellets. For uncrushed samples, the surface was grounded off before measurements.

The prepared samples were recorded with 0.2 mm and 1 mm slits whereas the former was placed closest to the sample. A step size of 0.041 ranging from 2θ = 20° - 100° was used, with a recording time set to 12 h 55 min. The samples were rotated during recording. Lattice parameters of the analyzed samples were determined by Pawley refinement using Topas software [36].

3.3.2 Mictrostructure and composition

The microstructure of the prepared samples were investigated in a SEM (Hitachi S-3400N) that was connected to an EDS-detector (Oxford X-max). The precursor mixture and the calcined samples were prepared for SEM characterization by dispersing one drop of the obtained milling slurry in 3-5 g of isopropanol. The diluted sample was then shaked before extracted with a pipette, and added onto a clean alumina stub. The sample stub was dried before being studied.

As for sintered pellets, they were first grinded with #1000 silicon carbide paper. And then polished with DiaPro diamond suspensions, using Plan, Dur, and Nap cloths with diamond size of 9 μm, 3 μm, and 1 μm, respectively. The polishing steps were finished by polishing the sample with a Chem cloth and surfactant solution. The pellets were then attached on an alumina stub with carbon tape before covering the outer area of the pellets with conductive tape, and coated with carbon.

Characterization of the samples were conducted wih secondary electron (SE) and backscatter electron (BSE) detectors. Low acceleration voltage (V_{ac} = 5-10 kV), low probe current, and short working distance ($\sim$ 5 mm) was used to secure high-resolution micrographs. EDS mapping was performed in AZtec software using high acceleration voltage (V_{ac} = 20 kV), high probe current, and $\sim$ 10 mm working distance. The collecting time was set to 5 min.

3.3.3 Density

The density of sintered samples were measured using Archimedes' method [35]. The method is based on the principle of immersing the ceramic body in a liquid and measure the volume from the buoyancy. This was executed by first gently grinding the pellet surfaces to remove loose particles from the surface, and rinsed with ethanol in ultrasonic bath. The pellets were then dried in an oven (110 $^\circ$ C, 1 - 2 h) and weighed. Next, the dry samples were placed in a sample holder and sealed in a vacuum exicator which was evacuated for air. The pressure was held at $\sim$ 0.0025 bar for 30 min, before isopropanol was introduced through a hose filling the sample holder. The samples were submerged in isopropanol at $\sim$ 0.0025 bar for 30 min, making sure that all open pores were filled, before introducing the exicator for atmospheric pressure.Temperature stabilization was achieved by submerging the samples for another 30 min. At last, the samples were weighed while immersed in isopropanol, and then in air after gently wiping the surface for excess isopropanol with a moist napkin. The density was calculated using equation 3.6

$$\rho_{sample} = \frac{m_{dry}}{m_{wet} - m_{sub}} \rho_{liq} \tag{3.6}$$

where m_{dry}, m_{wet}, m_{sub} are the weights of dry, wet, and submerged samples, respectively, while ρ_{liq} is the density of isopropanol.

The relative density, ρ_{rel} of the sample is then given by

$$\rho_{rel} = \frac{\rho_{sample}}{\rho_{BKT}} \cdot 100 \tag{3.7}$$

where ρ_{BKT} is 5.96 g/cm^3 [31].

3.3.4 Dielectric spectroscopy

Dielectric permittivity and electrical conductivity of sintered samples were measured with respect to temperature and frequency of the applied voltage. 10- mm diameter ceramic samples were prepared for dielectric measurements by first grinding the flat surface with #1000 silicon carbide paper, and then rinsed with ethanol in ultrasonic bath. Next, the pellets were sealed with tape, exposing only the flat surfaces. These samples where then coated in a gold sputter in Ar-atmosphere, with the current set to 15 mA for 15 min on each side.

Dielectric properties were measured using a frequency analyzer (Alpha-A high Performance Frequency Analyzer) that was connected to a heating unit (tubular furnace with Probostat). The samples were placed between two platina plates, which again was positioned between two platina electrodes. The platina electrodes were connected to a power source using platina wires. The sample and the electrodes were secured with a spring loaded alumina disc, and placed inside a sealed alumina tube. A controlled atmosphere of synthetic air (80 % O_2 and 20 N_2) were continuously supplied to the system. Next, the alumina tube was placed inside an isolated water cooled furnace with a thermocouple used to measure the temperature inside the alumina tube.

The probostat was set to four wire setup before usage. To confirm sufficient sample quality, all samples were measured over a wide range of frequencies before and after characterization. The actual characterization was conducted by measuring the dielectric properties of the samples every 30 seconds at frequencies $10^0 - 10^6$, with constant heating and cooling rate (120 $^\circ$ C/h) from room temper-

ature to 600° C (holding time at 600° C = 600 s).

3.3.5 Piezoelectric characterization

Polarization was measured with respect to applied electric field using an aix-ACCT TF Analyzer 2000. 10- mm diameter samples were prepared by first grinding the flat surface with #1000 silicon carbide paper until a $\sim$ 1 mm thick samples were obtained. Then the pellets were rinsed, sealed with tape, and coated with gold, as described in previous section.

Polarization of the samples were measured by applying bipolar electric fields with amplitudes from 1 to 70 kV/cm at room temperature. A step size of 10 kV/cm were used with 3-4 cycles for each field strength. The frequency was set to 0.25.

Chapter 4

Results

4.1 Preparation of BKT powder

4.1.1 Morphology

The SEM micrographs of the ball-milled precursor powder mixture and the calcined and ball-milled BKT powder prepared for this work are shown in Figure 4.1. The precursor powder mixture has a cube-like structure with an average particle size around 0.5 - 1 μm. Similarly, the calcined powder also has a cube-like structure, but with more rounded corners and with a smaller average particle size compared with the precursor powder.

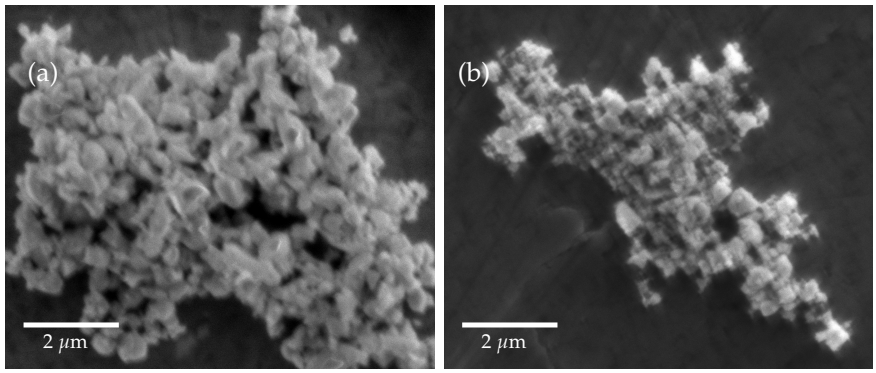

Figure 4.1: SEM micrographs; (a) precursor powder mixture; (b) calcined and ball-milled BKT powder. Both micrographs are taken with the same conditions.

Phase purity after calcination

An X-ray diffractogram of the calcined powder is presented in Figure 4.2. The diffraction peak (marked by *) at $\sim$ 30.5 $^\circ$ that appears after the first round of

calcination reveals the presence of a secondary phase. According to the PDF-database, the diffraction lines of $Bi_4Ti_3O_{12}$ (PDF card: 04-016-3435) provide a good match with the diffraction peaks of the secondary phase. By recalcining the powder, the secondary peak disappeared.

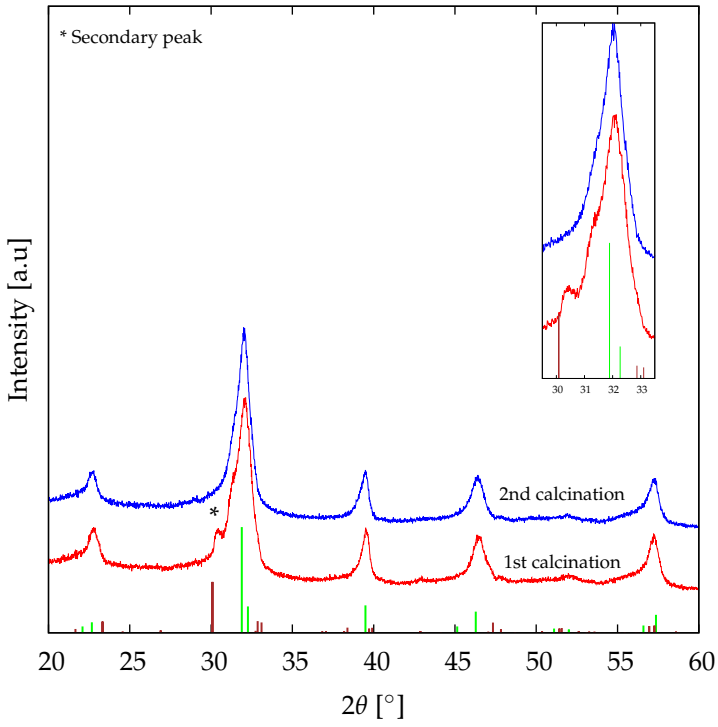

Figure 4.2: X-ray diffractograms of calcined BKT powder. The inset shows an enlarged image of the secondary peak at 30.5°. Reference diffraction lines are situated at the bottom; BKT (green, PDF card: 00-036-0339) and $Bi_4Ti_3O_{12}$ (brown, PDF card: 04-016-3435).

4.2 Preparation of sintered BKT

4.2.1 Phase purity and orientation

Nominal stoichiomtric BKT

A grinded and polished sample of the nominal stoichiometric BKT (BKT-0) is characterized in SEM, and the results are presented in Figure 4.3a and 4.3b. Micrographs were conducted with secondary (SE, left column) and backscatter (BSE, right column) electron detectors. It can be seen in the SE image that the sample possess dark secondary phase impurities. The secondary phases have rhombohedral-like and stick-shaped structure with size ranging from ~ 2 μm to ~ 10 μm. These observation are supported by the BSE image (Figure 4.3b), in which two different phases are seen, whereas the darkest phase is the secondary phase. Furthermore, the material is not fully densified, as small pores are seen thorughout the sample.

Table 4.1: The atomic composition of the stoichiometric and secondary phase in BKT-0 measured with EDS. The point mapping was conducted in the same area as in Figure 4.4 (marked x and *).

Element	**Stoichiometric phase*** **[atomic%]**	**Secondary phase^{x}** **[atomic%]**
Oxygen	54.37	58.30
Potassium	10.84	10.07
Titanium	22.97	31.34
Bismuth	11.81	0.29

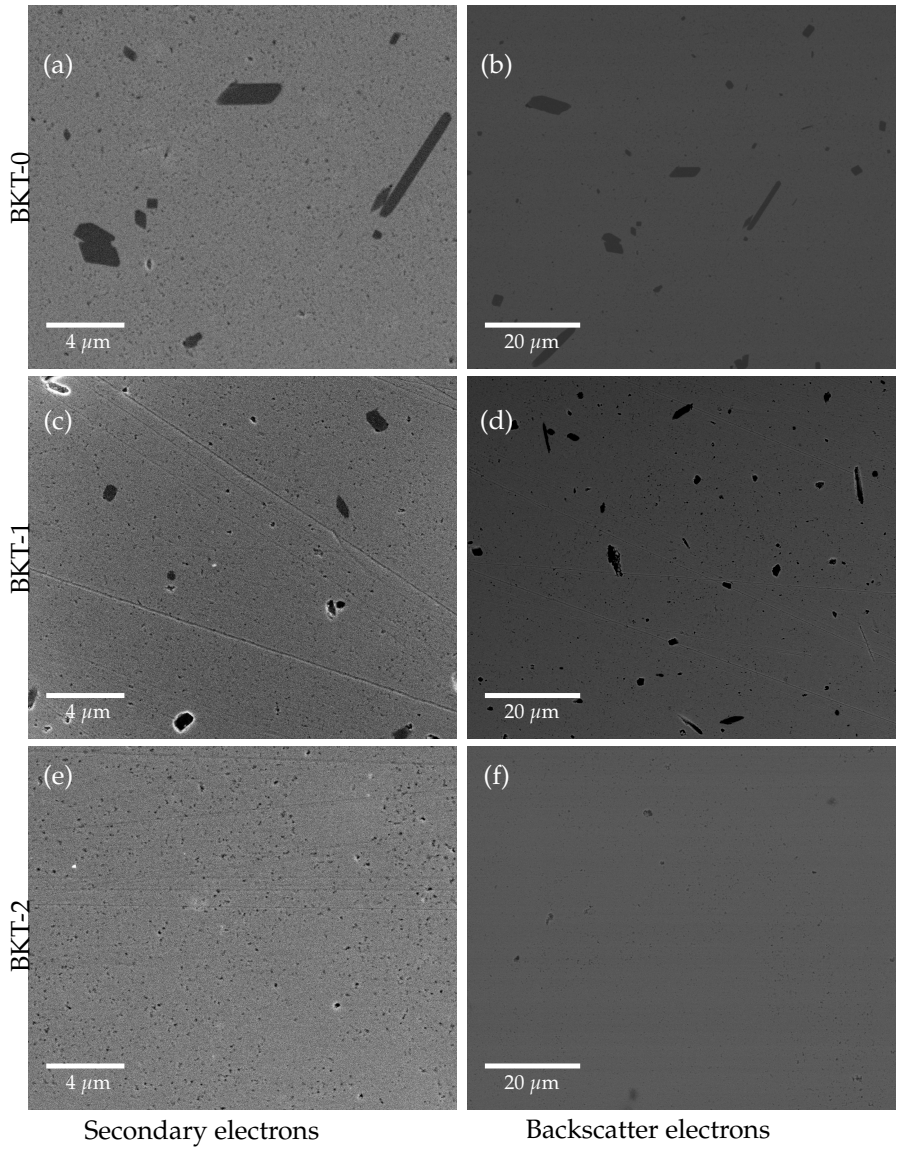

Figure 4.3: SEM micrographs of the polished sintered samples; (a) and (b) BKT-0; (c) and (d) BKT-1; (d) and (e) BKT-2. Dark secondary phases are seen in BKT-0 and BKT-1. Left column shows secondary electron images, while right column shows backscatter electron images. Pores are observed in all samples. Note different scales.

The observed secondary phases were further quantitatively analyzed with EDS mapping, shown in Figure 4.4. An arbitrary area of BKT-0 was chosen for the mapping. The resulting composition is summerized in Table 4.1. In Figure 4.4, a potassium (A-cation) and titanium (B-cation) rich phase is observed. In contrast, the mapping reveals that bismuth (A-cation) is not present. The atomic composition of the secondary phase was determined to have approximately 1:3 A:B stoichiometry.

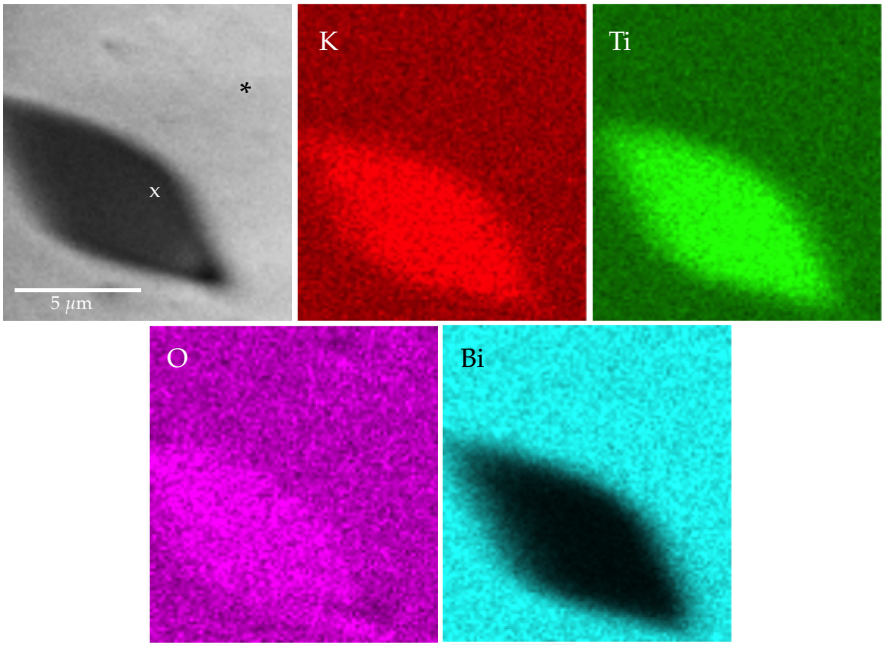

Figure 4.4: EDS mapping of nominal stoichiometric BKT showing the atomic distribution of the dark secondary phase. The compositions of marked areas (x and *) are listed in Table 4.1.

XRD scans of BKT-0 were conducted for an uncrushed and a crushed (and annealed) sintered sample, as shown in Figure 4.5a and 4.5b, respectively. Both diffractograms are indexed to the tetragonal crystal symmetry. However, the results obtained from uncrushed sample and crushed sample are slightly different from each other. The X-ray diffractograms of crushed sammple shows broaden peaks at $\sim 22^{\circ}$ and $\sim 57^{\circ}$, which correspond to the pseudocubic (100)

and (211) reflections, respectively. The X-ray diffractograms of the uncrushed sample shows that the pseudocubic (100) reflection is split into the tetragonal (100) and (001) reflections; and the pseudocubic (211) reflection is split into the tetragonal (112) and (211) reflections. Furthermore, no secondary phases are detected in the diffractogram. This is not in accordance with the secondary phases which are observed in SEM (Figure 4.3).

BKT with excess A cations

Sintered samples of BKT with excess bismuth and potassium (A cations) were synthesized from the calcined powder. These samples were prepared with 1 mol% (BKT-1) and 2 mol% (BKT-2) of excess A cations.

Scanning electron micrographs (SE and BSE) of the modified samples were compared with the micrographs of BKT-0. These are presented in Figure 4.3. From the images, it can be seen that the number and size of the secondary phases decrease as a response to the introduced A cations. Furthermore, no secondary phases are observed in the micrograph of BKT-2 (Figure 4.3e). As for the pores, no significant differences are seen between the different compositions. They are all small in size and uniformly distributed throughout all the samples, indicating that the ceramics are not fully dense.

X-ray diffractograms of the uncrushed and crushed (and annealed) sintered samples, of BKT with excess A cations are compared in Figure 4.5a and 4.5b. The resulting diffractograms show similar diffraction peaks to that observed for BKT-0. In other words, all the samples can be indexed to the tetragonal crystal structure. The X-ray diffractograms of the uncrushed samples show larger splits of the reflections compared to the ones of crushed samples. Furthermore, in the inset of Figure 4.5a, it is observed that the compositions with excess A cations have a slightly larger split between the tetragonal (002) and (200) reflections compared with undoped BKT-0. The secondary phases observed in the SEM images (Figure 4.3) are not detected in the corresponding diffractograms.

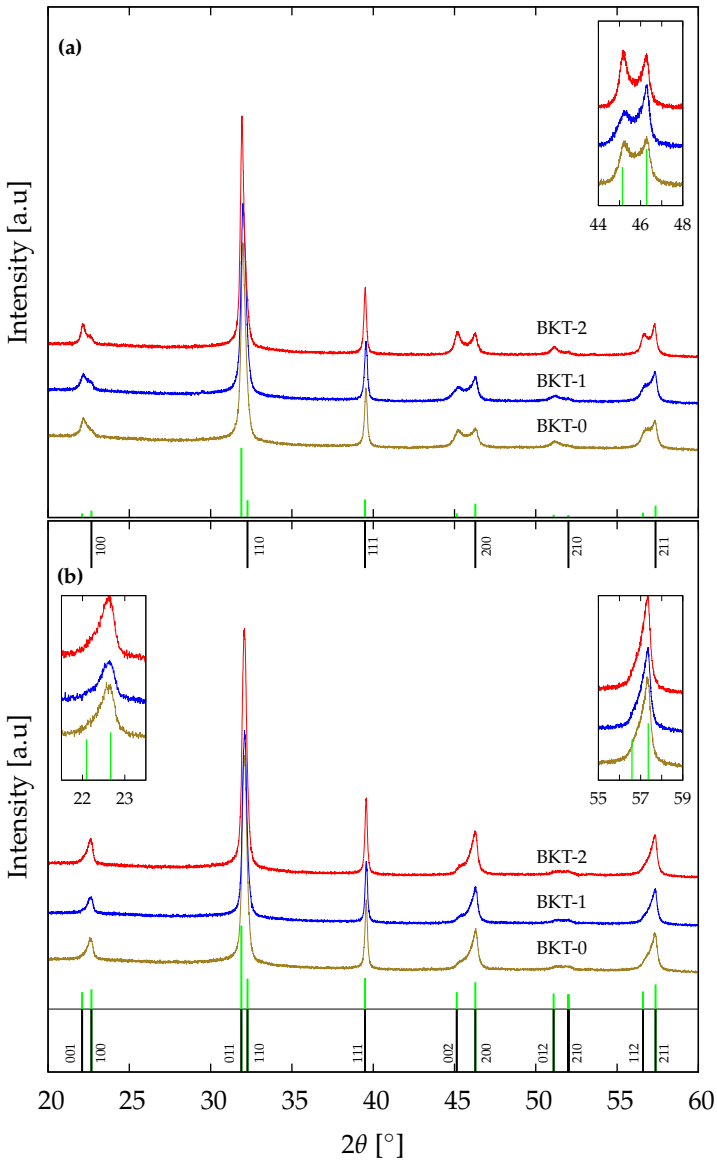

Figure 4.5: X-ray diffractograms of sintered samples of BKT-0, BKT-1, and BKT-2: (a) sintered samples; (b) crushed and annealed samples. The lower diffraction lines refer to tetragonal BKT (green, PDF card: 00-036-0339). Upper indices in (b) refer to cubic BKT. The insets show enlarged images of the diffraction peaks at 22.5°, 46°, and 57°.

CuO doping

In this section, samples of BKT with 2 mol% excess A cations (BKT-2) were doped with various amounts of CuO. These samples are prepared with 0.3 mol% (BKTC-0.3), 0.6 mol% (BKTC-0.6), and 0.9 mol% (BKTC-0.9) CuO doping, respectively.

Grinded and polished samples were analyzed in SEM and are compared in Figure 4.6. A redevelopment of secondary phases are observed with respect to the increasing amount of CuO. The shapes of these secondary phases are rhombohedral-like, which are very similar to the ones found in BKT-0 and BKT-1 (Figure 4.3). This observation suggests that the secondary phases seen in Figure 4.3 and 4.6 could be identical. It is, however, observed that 0.3 mol% of CuO doping does not seem to affect the phase purity of BKT, as no impurities are detected. Further analysis show that BKT-2 has more pores than the CuO doped compositions. Contrary, BKTC-0.3 seems to be well densified without much residual porosity. As for BKTC-0.6 and BKTC-0.9, some areas contain more pores than others. Unlike BKT-2, the porosity in these materials are not equally distributed throughout the sample.

XRD scans were conducted on uncrushed and crushed (and annealed) sintered samples of Cu-doped compositions. These are presented in Figure 4.7a and 4.7b, respectively. Regardless of the CuO content, these samples show similar diffraction pattern as the undoped materials. For this reason, the diffraction pattern of the CuO doped compositions are indexed to the tetragonal structure; in which the X-ray diffractograms of the uncrushed samples show larger splits between the reflections compared to the crushed samples. Similar to the other prepared materials, no secondary peaks are seen in the X-ray diffractograms, which is not in accordance with the SEM images (Figure 4.6).

Figure 4.8 presents the unit cell parameters of the CuO doped compositions obtained in *Topas* software [36]. Pawley fitting was conducted for each composition, using the X-ray diffractograms in Figure 4.7b. The lines correspond to the linear regression estimated for each parameter. For the a and c parameters, a slight increase is observed with respect to increasing CuO content. Furthermore,

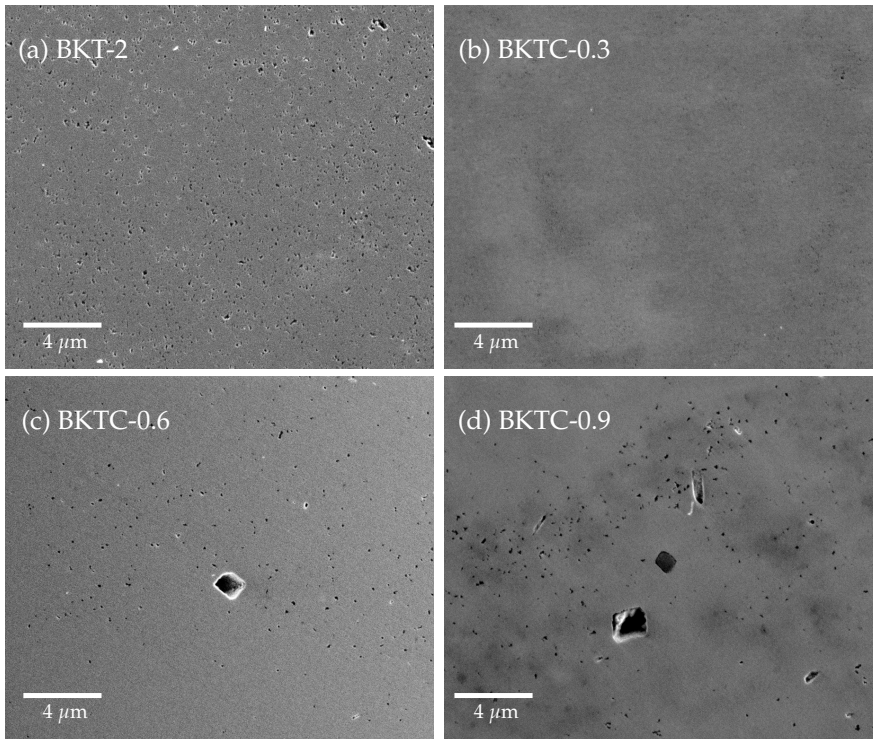

Figure 4.6: SEM micrographs of the polished sintered CuO doped samples; (a) BKT-2; (b) BKTC-0.3; (c) BKTC-0.6; and BKTC-0.9. Dark secondary phases are observed in BKTC-0.6 and BKTC-0.9. More pores are observed in BKT-2 compared to the other compositions.

the plot of c/a versus CuO doping, indicates that the crystal structure becomes more tetragonal with respect to CuO addition. The a and c parameters are given in Table 4.2.

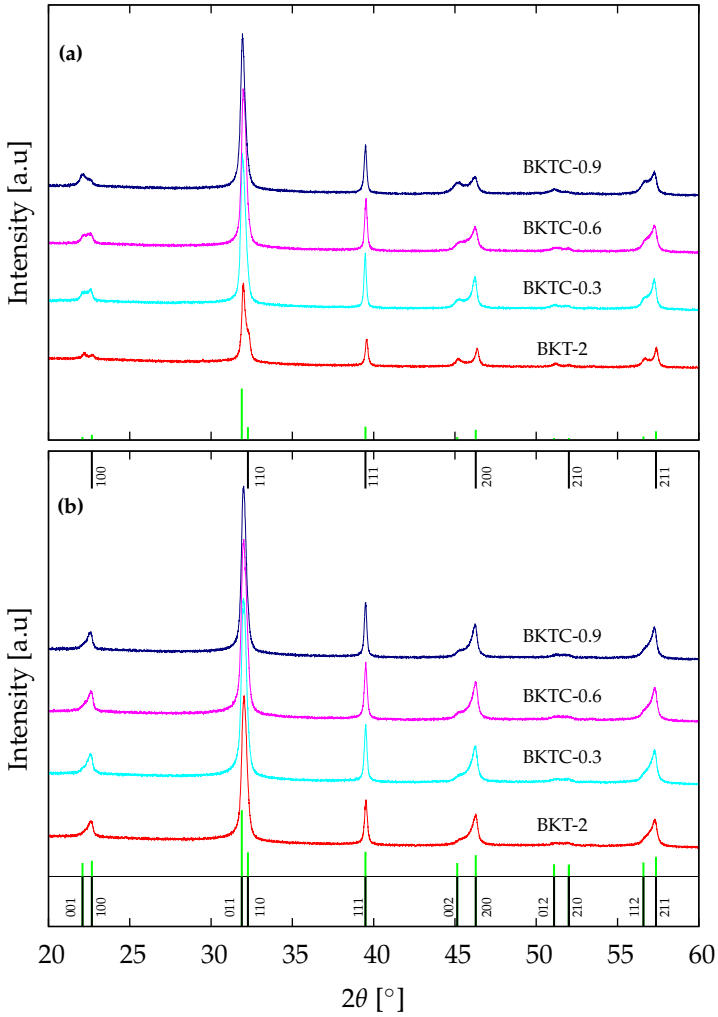

Figure 4.7: (X-ray diffractograms of sintered samples of BKT-2, BKTC-0.3, BKTC-0.6, and BKTC-0.9: (a) sintered samples; (b) crushed and annealed samples. The lower diffraction lines refer to tetragonal BKT (green, PDF card: 00-036-0339). Upper indices in (b) refer to cubic BKT.

Table 4.2: Unit cell parameters, piezoelectric, and dielectric data for the CuO doped BKT materials system obtained in this work.

Composition	**a** [Å]	**b** [Å]	$\mathbf{P_{max}}$[1], [μ**m/cm**^{2}]	$\epsilon'_{\mathbf{max}}$ **@ 1000 kHz**
BKT-2	3.930	3.983	-	1407 (451° C)
BKTC-0.3	3.931	3.985	7.1	1709 (401° C)
BKTC-0.6	3.929	3.987	-	1481 (408° C)
BKTC-0.9	3.932	3.988	8.5	1609 (440° C)

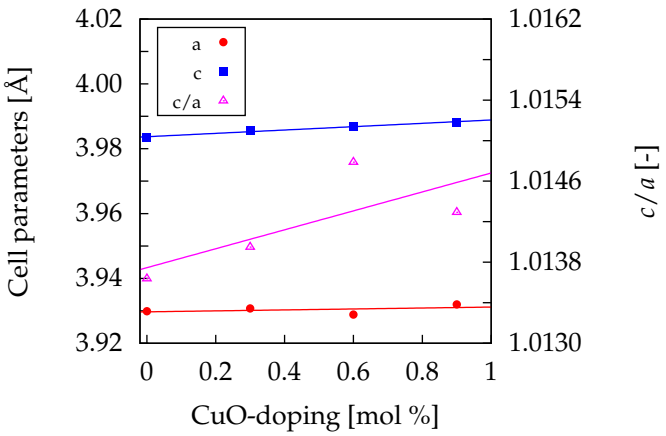

Figure 4.8: Unit cell parameters versus CuO addition, obtained by Pawley fitting of the X-ray diffractograms of Figure 4.7b. The c/a ratio is plotted against the CuO content in the right y-axis. The lines corresponds to the linear regression estimated for each parameter.

4.2.2 Density

The relative densities of the different compositions are summerized in Table 4.3, given as a percentage of the theoretical density of BKT [31]. The green body density of the modifed samples were determined by geometrical measurements. In these measurements, the samples proved to have a green density that varies from 60 % to 64 %.

The relative density of the sintered pellets were measured using Archemedes' method. The density plotted against addition of excess A cations are presented in Figure 4.9a, while the density plotted against addition of CuO are presented in Figure 4.9b. The relative density obtained for BKT-0 is 92.1 %, as shown in Figure 4.9a. Furthermore, no significant changes in the relative density is observed with respect to the introduction of A cations. This is in accordance with the SEM micrographs of the corresponding samples (Figure 4.3).

In contrast, a notable increase in relative densities are observed for the samples with CuO addition, which is observed in Figure 4.9b. Addition of 0.3 mol% CuO increased the density from 91.9 % to 95.8 %. However, no further increase was observed for samples with higher dopant level.

Table 4.3: Density of the different compositions determined by geometrical measurements (green density) and by Archimedes method' (sintered) in isopropanol. Theoretical density of BKT is obtained from Wefring et al. [31]

Composition	**Green [%]**	**Sintered [%]**
BKT-0	59.7	92.1 ± 0.5
BKT-1	63.4	92.1 ± 1.2
BKT-2	63.2	91.9 ± 1.2
BKTC-0.3	64.1	95.8 ± 0.3
BKTC-0.6	62.4	94.5 ± 1.4
BKTC-0.9	62.4	95.2 ± 1.2

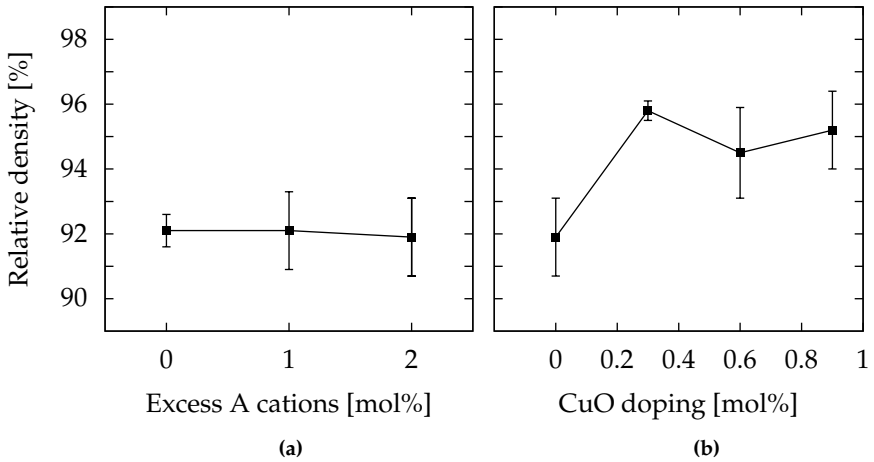

Figure 4.9: The relative density of BKT; (a) with excess A cations; (b) and with CuO doping. The relative density is measured by Archimedes' method. Theoretical density of BKT is obtained from Wefring et al. [22].

4.2.3 Piezoelectric and dielectric properties

Hysteretic behavior

The hysteresis loops, which is polarization plotted against electric field, of BKTC-0.3 and BKTC-0.9 are presented in Figure 4.10[2]. The hysteresis loop for both samples are similar in shape. It is observed that the hysteresis loop of BKTC-0.9 has the widest and most open shape, as well as possessing the highest values of remnant polarization, maximum polarization and coercive field. The maximum polarization ($P_{\max}$) of BKTC-0.3 and BKTC-0.9 are determined to be 8.5 μm/cm^2 and 7.1 μm/cm^2 at 70 kV/cm. The values of $P_{\max}$ are given in Table 4.2.

Relative dielectric permittivity

The relative dielectric permittivity, ϵ', of the CuO doped compositions were investigated with respect to temperature and frequency. A small deviation was

[2]Note that the polarization curve for BKT-2 and BKTC-0.6 were not measured in this work due to problems with the laboratory instruments.

observed between the heating and cooling curves due to latency in the temperature measurement versus the actual temperature of the samples. This effect is less distinct during cooling. For this reason, the cooling curves (from 600° C to ∼25° C) are the most interesting part of these results. The heating curves is given in Appendix A.

Figure 4.11 shows an overview of the temperature dependency of ϵ' of the CuO doped samples for frequencies from 1 kHz to 1000 kHz. All compositions show relaxor ferroelectric behavior as a broaden permittivity maximum (ϵ'_{max}) were observed at 400 - 450° C. This signifies the ferroelectric-paraelectric phase transition. Furthermore, it is observed that the corresponding temperature of ϵ'_{max} decreases with respect to decreasing frequency for all samples. A slight difference is observed between the undoped BKT-2 and the CuO doped samples as the former seems to have more flattened curves. A rapid increase of ϵ' in the higher temperature region is observed for all samples measured at 1 kHz. These curves do not correlate with the other frequencies. The maximum value of ϵ'_{max} (at 1000 kHz) is given in Table 4.2.

Figure 4.11e compares the relative permittivity of the different samples, measured at 1000 kHz. Here, it is observed that BKT-2 has the lowest ϵ'_{max} as well as the highest temperature of ϵ'_{max}, corresponding to 451° C. No correlation in ϵ' is observed among the CuO doped compositions.

Electrical conductivity

The conductivity measurements were conducted simultaneously with the dielectric measurements. For the same reason as stated in previous section, the cooling curves will be the main focus for further discussion. The electrical conductivity of the CuO doped samples were investigated with respect to temperature (from 600° C to ∼25° C) and frequency. The heating curves is given in Appendix A.

Figure 4.12 presents the conductivity for frequencies measured from 0.1 kHz to 100 kHz. At temperatures below 300 ° C, the alternating current (AC) dominates as the conductivity is frequency-dependent. However, at higher temperatures, the direct current (DC) is the dominating one, as the conductivity is independent

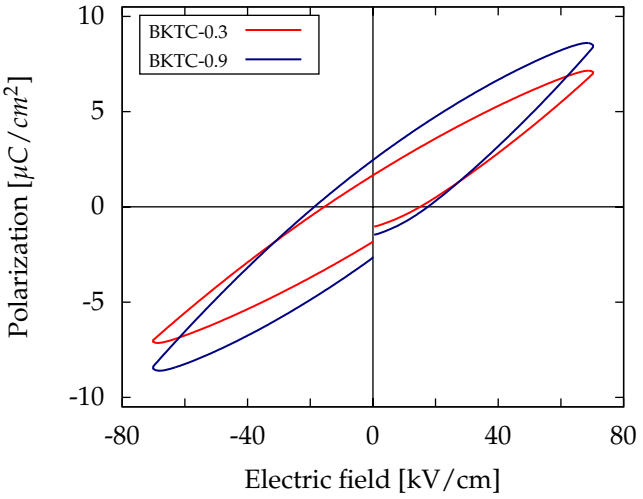

Figure 4.10: Bipolar polarization hysteresis loop for the investigated Cu-doped samples, obtained at 70 kV/cm^2 and 0.25 Hz.

of frequency. For all the samples measured at 0.1 kHz, the slope becomes steeper with increasing temperature. As for the samples measured at 100 kHz, a small rise is observed around 350° C (inset in Figure 4.12c). In Figure 4.12e, the various compositions measured at 10 kHz are compared. The conductivity is lowest for the undoped BKT. Moreover, no correlation is seen among the CuO doped compositions.

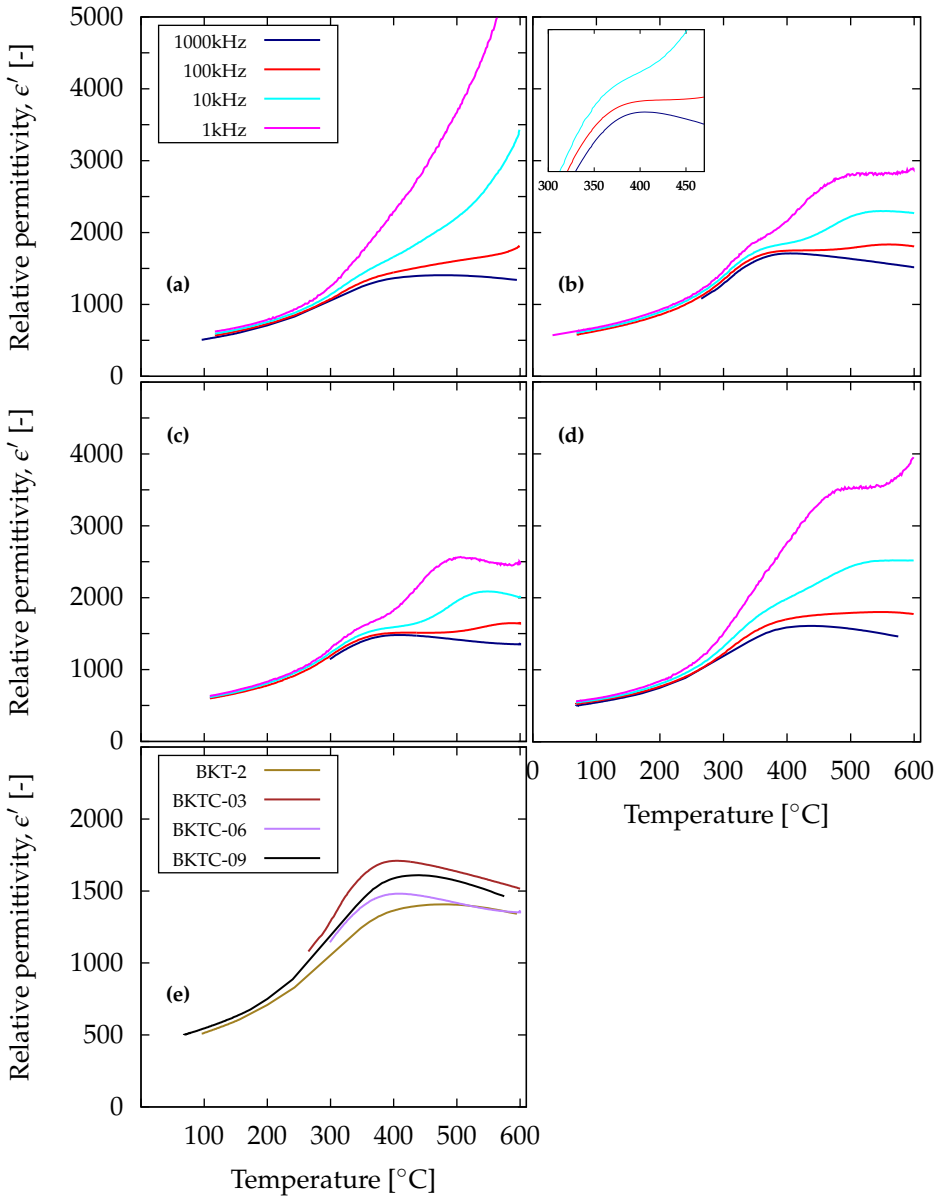

Figure 4.11: The relative dielectric permittivity for: (a) BKT-2; (b) BKTC-0.3; (c) BKTC-0.6; (d) BKTC-0.9; and (e) which presents the different compositions at 1000 kHz, as a function of frequency and temperature.

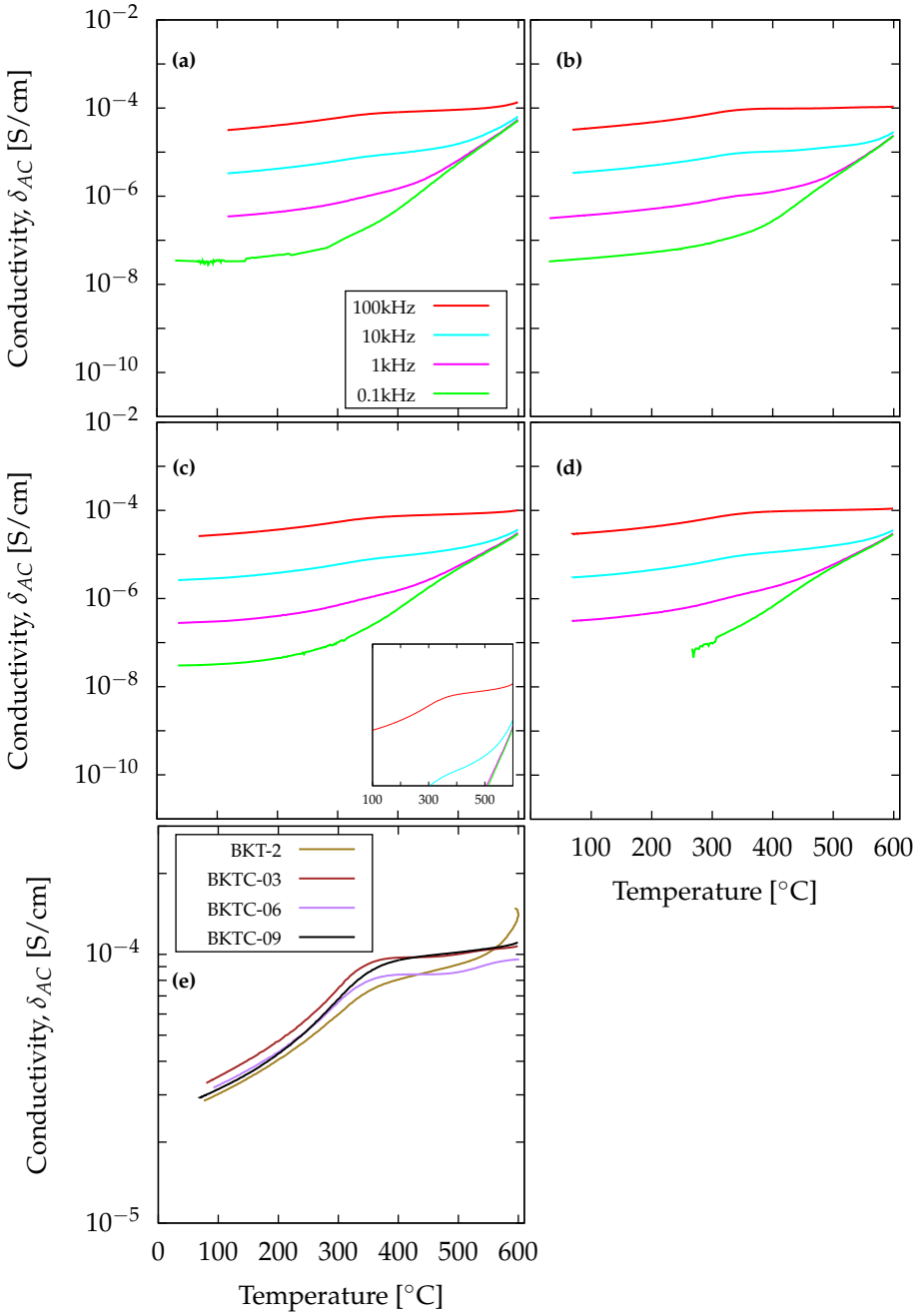

Figure 4.12: The electrical conductivity (σ_{AC}) for: (a) BKT-2; (b) BKTC-0.3; (c) BKTC-0.6; (d) BKTC-0.9; and (e) which presents the different compositions at 100 kHz, as a function of frequency and temperature. Note that the y-axis have logaritmic scale. Another unit is also used for (e).

Chapter 5

Discussion

To do (??)

5.1 Phase purity and stoichiometry of BKT

There are some distinct differences between the nominal stohichiometric sintered BKT samples prepared in this work, compared to the nominal stoichiometric sintered samples obtained by Wefring et al. [31]. Both studies were conducted with the conventional solid state synthesis, as described in Section 2.5. In the present work, however, a titanium rich/bismuth deficient secondary phase was detected in the BKT ceramic when the sample was investigated with EDS mapping, as shown in Figure 4.4. The quantitative measurements indicate that in some regions of the material, the expected 1:1 A:B stochiometry is in reality shifted towards approximately 1:3, and thus resulting in titanium rich (or B-rich) secondary phases. It is reported in the literature that the phase purity of BKT is difficult to attain [5, 7], which is the observed case also in this study. According to Hiruma et al. [5], the formation of $K_2Ti_6O_{13}$ secondary phases gradually increases in the sintering temperature range from 1040 to 1060 $^\circ$ C. This conclusion is to some extent in accordance with the EDS analysis conducted on BKT-0 (sintered at 1060 $^\circ$ C), as the acquired secondary phases correspond to a $K_2Ti_6O_{13}$-like compound (Table 4.1). Nevertheless, these B-rich secondary phases only represent a small percentage of the total mass as they were not detected in the X-ray diffractogram in Figure 4.5.

The shift in A to B stoichiometry is confirmed, as a significant change in the number of secondary phases is observed when excess A cations are introduced to the nominal stoichiometric samples, shown in Figure 4.3. It is observed that the number of B-rich secondary phases gradually decreases with respect to the increasing amount of added excess A cations. It can therefore be suggested that

the the nominal stoichiometric sample in reality lacks approximately 2 mol% of A cations (A-deficiency) as the ions seem to be fully solved into the perovskite structure.

A possible explanation for the A-deficiency might be that the mixture of reactant powders is inhomogeneous. As described in Section 2.5, a well-mixed sample with small particles is required, as the reaction is dependent on the diffusion rate. In this case, the development of agglomerations might have occured, although no significantly large particles/agglomerates were detected in the SEM images of the precursor and calcined powders in Figure 4.1.

In general, the formation of a B-rich phase would correspondingly also result in the formation of an A-rich phase in the powder mixture. This A-rich phase is confirmed, as a $Bi_4Ti_3O_{12}$-like secondary phase is detected in the calcined powder (Figure 4.2). It therefore seems reasonable that the A-rich phase in the calcined powder, and the B-rich phase in the sintered sample are connected. This implies that the calcined powder has three different phases present.

It is observed that the diffraction peak, which was accredited to a $Bi_4Ti_3O_{12}$-like secondary phase, disappears during the second round of calcination (Figure 4.2), suggesting that a complete reaction is reached. This could be associated with a slow diffusion and thus reaction rate. However, based on the assumption of a complete reaction, the B-rich phase should react with the A-rich phase, and consequently result in a phase pure material. This does not occur as only the B-rich phase is detected in the sintered sample, as seen in Figure 4.3.

As described in Section 2.4, it has been reported in earlier studies that the volatilization of A cations and oxygen anions at high sintering temperatures is the main reason for the formation of secondary phases and the poor sintereability of BKT ceramics [7, 37, 38]. The volatility of bismuth and potassium will accordingly shift the A to B ratio, as the material becomes A-deficient. It can be assumed that the perovskite structure is not capable of accommodating the vacancy levels associated with the deviaton from the ideal stoichiometry. In other words, the solubility of vacancies is low, which implies that the solution range of A to B non-stoichiometry is narrow. König et al. [7] described the thermal decomposi-

tion of BKT by suggesting that the evaporation of K_2O/Bi_2O_3 induces a shift of the nominal stoichiometric composition to a composition within a three-phase region involving K_2O, TiO_2, and Bi_2O_3. The shift will consequently lead to the formation of B-rich secondary phases in addition to BKT. This suggestion is in accordance with the observed case in this study.

In summary, the nominal stoichiometric sample of BKT is in reality A-deficient. The formation of secondary phases seems to be related to an inhomogeneous mixture of reactant powder, as well as the volatilization of A cations and oxygen anions during high temperature sintering.

5.2 Effect of copper doping

5.2.1 A to B occupancy

There are three possible scenarios upon addition of CuO to the BKT (BKTC-x, $x = 0.3 - 0.9$) perovskite structure, depending on which lattice site the copper ions prefer: (1) substitution of A cations; (2) substitution of B cations; (3) and compensation of A-cation vacancies. These scenarios are described with Kröger-Vink equations in Section 2.4.4.

If Cu^{2+} ions prefer substitution of Bi^{3+} or Ti^{4+} ions, it acts as an acceptor. Consequently, this would lead to a charge excess on the occupied site, which is compensated by the formation of oxygen vacancies, as presented in equation 2.11 and 2.12. If Cu^{2+} ions prefer the substitution of K^+ ions, it acts as a donor. The corresponding site then becomes charge deficient, which is compensated by the formation of potassium vacancies, shown in equation 2.10. The last possibility occurs if the Cu^{2+} ions prefer the vacant A-sites; leading to a reduction of the vacancy concentration in the material system, as described in equation 2.13 and 2.14. These scenarios will be further discussed below.

The ionic radius of the Cu^{2+} ion (0.73 Å) is smaller than the A cations (K^+: 1.64 Å, Bi^{3+}: 1.03 Å) and larger than the Ti^{4+} ion (0.60 Å) [11]. In general, this implies that the lattice parameters decrease when substituting into A-sites. Conversely, if Cu^{2+} substitute into B-sites, the lattice parameters will increase. Furthermore,

it has been reported that the formation of A cations and oxygen vacancies decreases the lattice parameters [39]; implying that the incorporation of Cu^{2+} ions into vacant A-sites increases the unit cell. In this study, the unit cell parameters, a and c, of the material slightly increase with respect to increasing CuO content, as presented in Figure 4.8. These findings therefore indicate that the Cu^{2+} ions either incorporates into the vacant A-sites or substitute for Ti^{4+} ions on the B-site. This suggest that scenario (2) and (3) described in the previous paragraph are most likely to occur.

It has been argued by Hagiwara et al. [11] in their work on BKT-BFO material system that Cu^{2+} ions incorporates into vacant A-sites. The hypothesis is based on two main observations; that the lattice constant increases with increasing dopant level, and that the polarization-electric field (P-E) hysteresis loop gradually opens with respect to increasing amount of CuO addition. The latter is an indication of a reduction of pinning centers caused by defect dipoles in the material, as described in Section 2.3 [11]. Based on Hagiwara et al.s [11] conclusion, and the strong similarities between BKT and BKT-BFO material systems, the incorporation of Cu^{2+} ions into the vacant A-sites seems like a probable scenario. This suggestion is further supported as the P-E hysteresis loop in Figure 4.10 becomes more open with respect to the increased CuO content. This indicates that the number of A cation and oxygen vacancies are reduced; resulting in the depinning of the P-E hysteresis loop, as illustrated in Figure 2.11.

Another possibility of site occupation is discovered when investigating the SEM images of BKTC-0.6 and BKTC-0.9 in Figure 4.3. These micrographs revealed the presence of the same rhombohedral secondary phases (B-rich) that was observed in BKT-0. The impurities seem to gradually return with respect to increasing CuO addition. Prior to the findings from the previous section, this observation indicates that the ideal A:B stoichiometry is shifted towards a B-rich region. In other words, the formation of secondary phases therefore suggests that the Cu^{2+} ions substitute for the Ti^{4+} ions on the B-sites; leading to excess Ti^{4+} ions in the material system. For this reason, B-rich secondary phases are developed, as the perovskite structure is not capable of solving the excess B cations associated with the substitution. Despite this observation, it can be argued that low level of dopants occupy the vacant A-sites as no secondary phase is observed in the

SEM micrographs of BKTC-0.3 in Figure 4.6b.

In the study of CuO-doped PZT and KNN, substitution occurs between the Cu^{2+} ions and the B-site cations (Cu^{2+} replaces Zr^{4+} / Ti^{4+} and Nb^{5+}, respectively) [8, 9, 40]. Accordingly, acceptor doping is compensated by the formation of oxygen vacancies. In general, this leads to the development of defect dipoles that correspondingly create domain wall pinning centers, as described in Section 2.3. The pinning effect stabilizes the domain structure and limits the domain wall movement; reducing the nonlinearity of P-E hysteresis loop. As a result, a pinched and a double P-E hysteresis loop are developed for CuO doped PZT and KNN, respectively [9, 40].

With respect to these studies, if Cu^{2+} ions substitute for Ti^{4+} on the B-sites, it is expected that a pinched P-E loop is developed. In this study, the opposite occured as the P-E hysteresis loop became more open with additional dopants. As already described, this indicates a reduction of the vacancy concentration; implying occupation of vacant A-sites. However, these results need to be interpreted with caution as piezoelectric measurements were only conducted on two compositions. Moreover, these observations do not suggest which A-site (bismuth or potassium) the ions prefer to occupy.

From the discussed results above, It is therefore believed that copper compensates A-cation vacancies on A-site as well as substituting with titanium on B-sites in CuO doped BKT.

5.2.2 Crystal phase of modified BKT materials

The X-ray diffractograms (Figure 4.5 and 4.7) of all the samples are indexed to the tetragonal *P*4*mm* perovskite structure, which is in accordance with the literature [5, 29]. However, the results obtained from uncrushed and crushed (and annealed) samples are slightly different from each other. The X-ray diffractograms of crushed samples provide broaden peaks at the pseudocubic (100) and (211) reflections. These diffraction patterns are similar to that obtained in previous reports [5, 31]. The X-ray diffractograms of the uncrushed samples, however, shows a larger split of the pseudocubic (100) and (211) reflections. These pseu-

docubic reflections are split into tetragonal (100) and (001); and tetragonal (112) and (211) reflections, respectively. The reason for this deviation is not clear. The samples were crushed and annealed above T_c to release potential mechanical stress/strain effects in the material. The broad peaks may indicate that some stress/strain effects still remain in the sample.

Pawley fitting was conducted on the X-ray diffractograms obtained from the crushed and annealed samples, as shown in Figure 4.8. The refined lattice parameters of BKT-2 were $a = 3.930$ Å and $c = 3.983$ Å, which slightly deviate with Wefring et al.s [31] reported values ($a = 3.933$ Å and $c = 3.975$ Å). The c/a ratio of the prepared materials increased with respect to the CuO addition. This implies that the tetragonality increases with the dopant content, suggesting a larger spontaneous polarization in the unit cell. However, these findings must be interpreted with caution as the refinement is not very accurate.

5.2.3 Piezoelectric and dielectric properties

The dielectric measurements of all the samples showed relaxor-like behavior with maximum permittivity (ϵ'_{max}) above 400° C, as presented in Figure 4.11. ϵ'_{max} corresponds to the pseudocubic-cubic phase transition in BKT shown in Figure 2.13. Furthermore, it is observed that the given temperature of ϵ'_{max} (T_m) declines with respect to decreasing measured frequency, which is also typical characteristic of relaxors.

In this study, the temperature dependency of ϵ' for the undoped BKT-2 (Figure 4.11e) has the broadest phase transition and the smallest ϵ'_{max} among all the compared samples. It has been stated that perovskite ferroelectrics with higher content of A-site vacancies exhibit a broader phase transition and a smaller ϵ'_{max}. According to Bidault et al. [39], this is related to the reduced long-range polar ordering. It can therefore be indicated that BKT-2 has the largest amount of A-site vacancies. In CuO-doped BKT, the higher values of ϵ'_{max} and the sharper phase transition imply that the introduced Cu^{2+} ions compensate the vacant A-sites to create longer polar ordering. This observation further support the hypothesis about A-deficiency in BKT materials, as discussed in Section 5.1. It is, however, observed that no correlation is observed among the CuO-doped samples.

The values of the relative permittivity, ϵ', obtained in this study, did not match the values acquired for BKT in the literature [5, 41]. Moreover, it is seen that the low frequency plots show a steady increase of ϵ' in the higher temperature region. This behavior might indicate too high conductivity, and is especially evident for BKT-2. This is also confirmed as the material possesses the lowest conductivity among the measured samples (Figure 4.12e). The low electrical resistivity of the prepared samples is further confirmed as the conductivity for undoped BKT-2 (lowest of all the samples, see Figure 4.12e) obtained in this work, is higher than what was achieved by Wefring et al [31], as shown in Figure 5.1. In the conductivity measurements at 100 kHz, a slight peak is observed around 300° C. This probably occurs due to tetragonal-cubic phase transition.

In the piezoelectric measurements, BKTC-0.9 obtained the largest value of maximum polarization of 8.5 μm/cm$_2$ at 70 kV/cm^2. This is lower than the values presented in previous reports [31, 42]. A possible explanation might be that the conductivity (Figure 4.12) found in these materials are too high, as suggested in Figure 5.1.

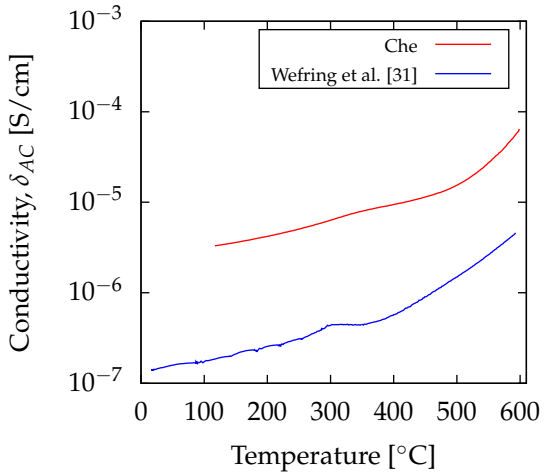

Figure 5.1: Conductivity plotted against temperature, obtained by the author and Wefring et al. [31]

5.2.4 Density of BKT materials

It has been noted in other studies that the preparation of a dense BKT ceramic is difficult without special techniques such as the hot isostatic pressing [5, 43]. However, BKT ceramics with a density of 97 % of theoretical density were successfully synthesized by Wefring et al. [31] using the conventional solid state synthesis. An identical fabrication route was used for this work, but a notably lower relative density (even with a green body density of $\sim$ 60%) was obtained for BKT-0 (92 %), as shown in Figure 4.9. One possible explanation may be that the low density is connected to the secondary phases found in the material system. These impurities might hinder grain growth during high temperature treatments. It has been suggested that the addition of excess bismuth might suppress microcracks and enhance the grain growth [44]. However, this is not the observed case in this work, as no significant increase in the relative density was achieved for the phase pure BKT-2.

In Figure 4.9, it is observed that the CuO addition promotes the densification of BKT. The distinct increase in relative density when going from the undoped BKT-2 (92 %) to CuO-doped BKTC-0.3 (96 %) suggests that CuO acts as a sintering aid when added to BKT. This assumption is in agreement with other studies [9, 10, 11] were CuO is known for having a positive impact on the densification of different ceramic materials. This is due to the formation of a liquid phase at the sintering temperature. The liquid phase increases the density by wetting the solid, providing a capillary force that drag the grains together. Moreover, the viscous flow increase the transport rate responsible for grain coarsening and densification [45]. Note, however, that the effect is most evident for small amounts ($<$ 0.3 mol%) of CuO as the relative density seems to be unaffected by further addition. It can therefore be suggested that a saturation limit occurs at approximately 0.3 mol% CuO addition.

The SEM images of BKTC-0.6 and BKTC0.9 (Figure 4.6c and 4.6d) show that the pores are not equally distributed, as some ares contain more pores than others. This indicates that the samples are inhomogeneous, which is in accordance with the discussed case in Section 5.1.

Chapter 6

Concluding remarks and further work

In this work, BKT ceramics with 0 - 2 mol% of excess A-cations, and 0.3 - 0.9 mol% of CuO (BKTC-x, $x = 0.3 - 0.9$) additives, have been prepared using the conventional solid state synthesis. The preparation of nominal stoichiometric BKT (BKT-0) results in a small degree of B-rich secondary phases. These secondary phases are removed by the addition of 2 mol% of excess A-cations, confirming that BKT-0 is A cation deficient.

The density obtained for BKT-0 is 92 % of the theoretical density. This value is not increased with the addition of excess A-cations. BKT with 0.3 mol% of CuO addition achieves the highest density and are measured to be 96 %, while the corresponding values for BKTC-0.6 and BKTC-09 are 94 % and 95 %, respectively. This proves that CuO acts as a sintering aid at low concentration of dopant.

The structural characterization of all investigated materials shows that the materials are indexed to the tetragonal perovskite structure, where the lattice parameters slightly increase with increasing CuO content. The dielectric measurements confirmed the relaxor-like behavior as a broadening of the maxiumum relative permittivity, ϵ'_{max}, at the ferroelectric to paraelectric phase transition are observed for all compositions. Moreover, the temperature of ϵ'_{max} decrease with decreasing frequency. The value of the relative permittivity of CuO doped materials are found to be higher compared with the undoped BKT-2. The piezoelectric measurements show that BKTC-0.9 develops the most open P-E hystereses loop obtaining the largest maximum polarization of 8.5 μm/cm^2, while the more narrow P-E hystereses loop of BKTC-0.3 obtained a value of 7.1 μm/cm^2. The SEM images of the CuO doped samples shows that the B-rich secondary phases gradually redevelops with the increasing CuO content. From these results, it is

suggested that the Cu^{2+} ions both reduces the vacancy concentration by incorporating into vacant A-sites, and substitute the Ti^{4+} ions on B-site.

The results from this study provided some information about the effect of CuO doped BKT. For further work, the BKT materials should be prepared with higher density and without secondary phases to achieve more consistent data, as well as lowering the conductivity of the materials. The A-site occuppancy (bismuth and potassium site) should also be further investigated as this was not understood in this work.

Appendices

Appendix A

Dielectric measurements

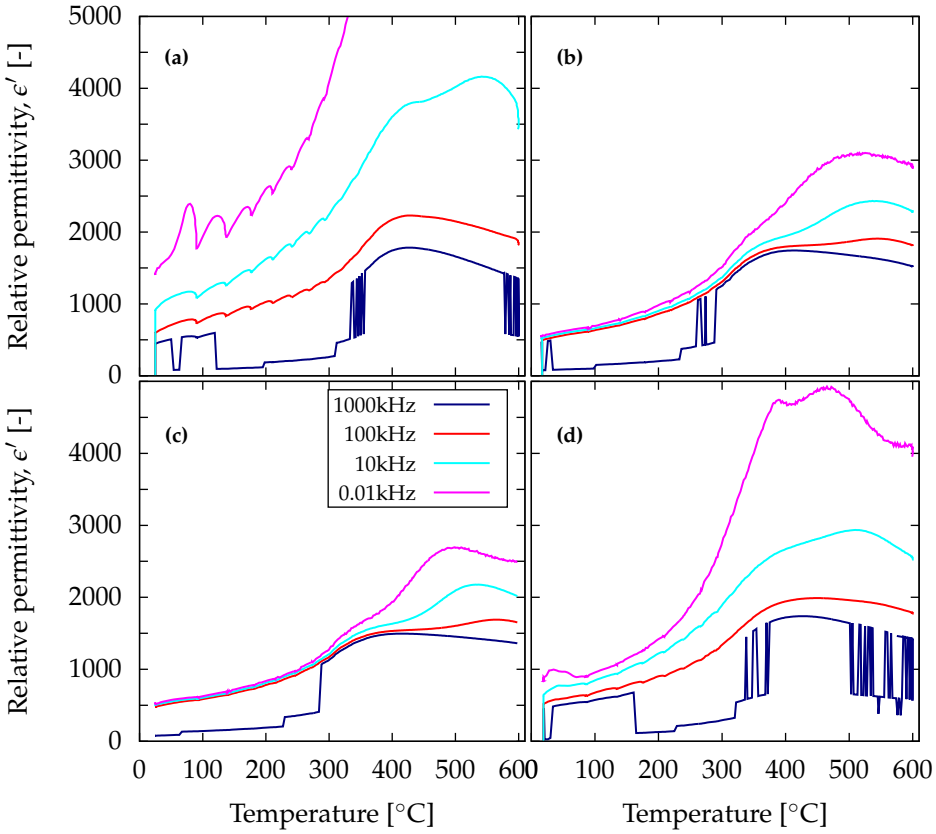

Figure A.1: The relative dielectric permittivity for: (a) BKT-2; (b) BKTC-0.3; (c) BKTC-0.6; (d) BKTC-0.9, as a function of frequency and temperature (heating curves, 25° C to 600° C). The experimental data are incosistent due to noise.

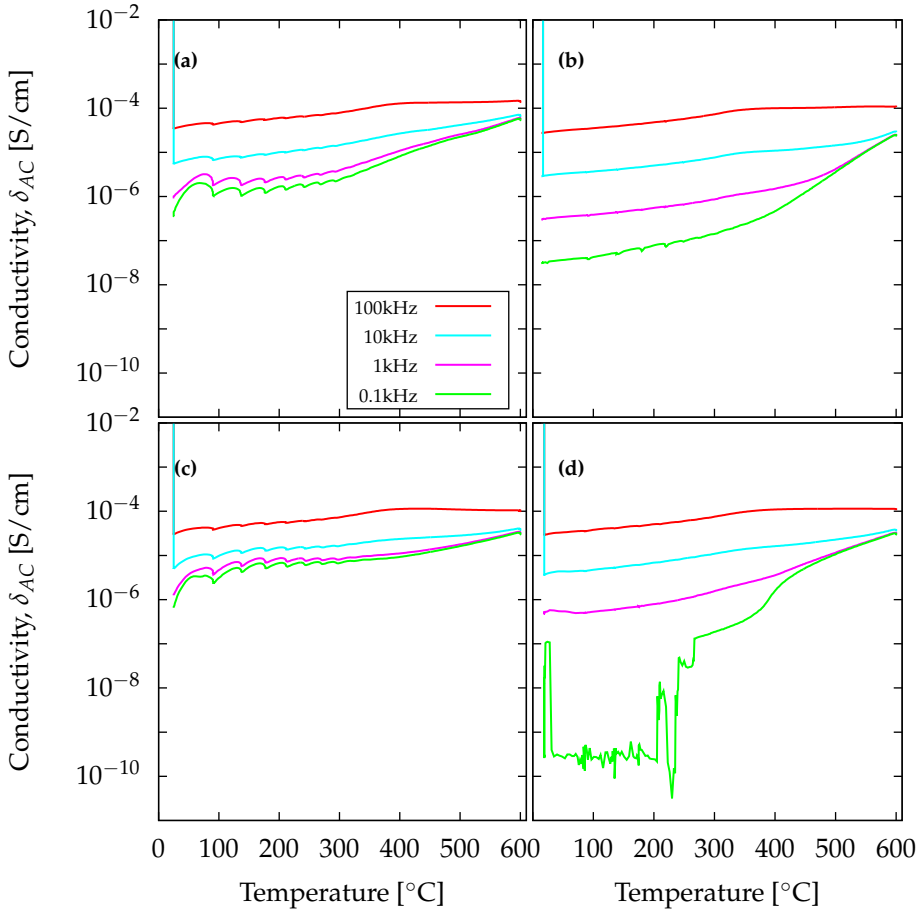

Figure 6.2: The electrical conductivity (σ_{AC}) for: (a) BKT-2; (b) BKTC-0.3; (c) BKTC-0.6; (d) BKTC-0.9, as a function of frequency and temperature (heating curves, 25° C to 600° C). The experimental data are incosistent due to noise. Note that the y-axis have logaritmic scale.

Bibliography

[1] B. Jaffe, Wi R. Cook, and H. Jaffe. *Piezoelectric Ceramics*. Academic Press London and New York, 1971.

[2] G. H. Haertling. Ferroelectric Ceramics: History and Technology. *Journal of the American Ceramic Society*, 82(4):797–818, 1999.

[3] J. Roedel, W. Jo, K. Seifert, E. Anton, T. Granzow, and D. Damjanovic. Perspective on the Development of Lead-free Piezoceramics. *Journal of the American Ceramic Society*, 92(6):1153–1177, 2009.

[4] Directive 2002/95/EC of the European Parliament and of the Council on the restriction of the use of certain hazardous substances in electrical and electronic equipment. *Official Journal of the European Union*, 2003.

[5] Y. Hiruma, R. Aoyagi, H. Nagata, and T. Takenaka. Ferroelectric and Piezoelectric Properties of $Bi_{0.5}K_{0.5}TiO_3$ Ceramics. *Japanese Journal of Applied Physics*, 44(7A):5040–5044, July 2005.

[6] M. I. Morozov, M.-a. Einarsrud, T. Grande, and D. Damjanovic. Lead-Free Relaxor-Like $0.75Bi_{0.5}K_{0.5}TiO_3$ – $0.25BiFeO_3$ Ceramics with Large Electric Field-Induced Strain. *Ferroelectrics*, 439(1):88–94, January 2012.

[7] J. König, M. Spreitzer, B. Jančar, D. Suvorov, Z. Samardžija, and A. Popovič. The Thermal Decomposition of $Bi_{0.5}K_{0.5}TiO_3$ Ceramics. *Journal of the European Ceramic Society*, 29:1695–1701, 2009.

[8] P Jakes, H Kungl, R Schierholz, and R Eichel. Analyzing the Defect Structure of CuO-Doped PZT and KNN Piezoelectrics From Electron Paramagnetic Resonance. 61(9):1447–1455, 2014.

[9] D Lin, K. W. Kwok, and H. L. W. Chan. Double Hysteresis Loop in Cu-doped $K_{0.5}Na_{0.5}NbO_3$ Lead-free Piezoelectric Ceramics. *Applied Physics Letters*, 90(23):232903, 2007.

[10] C. Chou, C. Liu, C. Hsiung, and R. Yang. Preparation and Characterization of the Lead-free Piezoelectric Ceramic of $Bi_{0.5}Nai_{0.5}TiOi_{0.5}$ doped with CuO. *Powder Technology*, 210(3):212–219, July 2011.

[11] M Hagiwara and S Fujihara. Effects of CuO Addition on Electrical Properties of $0.6BiFeO_3$ -$0.4Bi_{0.5}K_{0.5}TiO_3$ Lead-Free Piezoelectric Ceramics. *Journal of the American Ceramic Society*, 98(2):469–475, 2015.

[12] J. Luxová, P. Šulcová, and M. Trojan. Study of Perovskite Compounds. *Journal of Thermal Analysis and Calorimetry*, 93(3):823–827, October 2008.

[13] V. M. Goldschmidt. Die Gesetze der Krystallochemie. *Die Naturwissenschaften*, 14(21):477–485, 1926.

[14] S Tidrow. Mapping Comparison of Goldschmidt's Tolerance Factor with Perovskite Structural Conditions. *Ferroelectrics*, 470(1):13–27, 2014.

[15] D. Damjanovic. Piezoelectric Properties of Perovskite Ferroelectrics: Unsolved Problems and Future Research. *Annales de Chimie Science des Matériaux*, 26:99–106, 2001.

[16] T Yamamoto. Ferroelectric Properties of the $PbZrO_3$–$PbTiO_3$ System. *Japanese Journal of Applied Physics*, 35(1):5104–5108, 1996.

[17] R. Tilley. *Understanding Solids - The Science of Materials*. Wiley, 2004.

[18] D Damjanovic. Ferroelectric, Dielectric and Piezoelectric Properties of Ferroelectric Thin Films and Ceramics. *Reports on Progress in Physics*, 61(9):1267, 1999.

[19] Cross. Relaxor Ferroelectrics, 1987.

[20] A. A. Bokov and Z.-G. Ye. Recent Progress in Relaxor Ferroelectrics with Perovskite Structure. *Journal of Materials Science*, 41(1):31–52, January 2006.

[21] V. V. Shvartsman and D. C. Lupascu. Lead-Free Relaxor Ferroelectrics. *Journal of the American Ceramic Society*, 95(1):1–26, January 2012.

[22] Mads Jonas Christensen. On the Effect of A to B Stoichiometry Variation on Conductivity and Phase. (June), 2014.

[23] P Atkins, T Overton, J Rourke, M Weller, and F Armstrong. *Inorganic Chemistry*. Oxford, 5th editio edition, 2010.

[24] L Jin, F Li, and S Zhang. Decoding the Fingerprint of Ferroelectric Loops: Comprehension of the Material Properties and Structures. *Journal of the American Ceramic Society*, 97(33900):1–27, 2014.

[25] H. J. Vink and F. A. Kröger. Relations between the Concentrations of Imperfections in Crystalline Solids. *Solid State Physics*, 3:307–435, 1956.

[26] L. X. Zhang and X. Ren. In Situ Observation of reversible Domain switching in aged Mn-doped $BaTiOi_3$ Single Crystals. *Physical Review B - Condensed Matter and Materials Physics*, 71:1–8, 2005.

[27] G. H. Jonker. Nature of Aging in Ferroelectric Ceramics. *Journal of American Ceramic Society*, 55(January):57–58, 1972.

[28] C. F. Buhrer. Some Properties of Bismuth Perovskites. *The Journal of Chemical Physics*, 36(3):798, 1962.

[29] V. V. Ivanova, A .G. Kapyshev, Y. N. Venevtsev, and G. S. Zhdanov. X-ray determination of the symmetry of elementary cells of the ferroelectric materials $Bi_{0.5}K_{0.5}TiO_3$ and $Na_{0.5}Bi_{0.5}TiO_3$ and of high-temperature phase transitions in $Bi_{0.5}K_{0.5}TiO_3$. *Izvestiya Akademii Nauk SSSR, Seriya Fizicheskaya*, 26:354–356, 1962.

[30] Y Saito, H Takao, T Toshihiko, N Tatsuhiko, T Kazumasa, H Takahiko, N Toshiatsu, and N Masaya. Lead-free Piezoceramics. *Physica Status Solidi B*, 432(November):1–4, 2004.

[31] E. T. Wefring, M. I. Morozov, M. Einarsrud, and T. Grande. Solid-State Synthesis and Properties of Relaxor (1-x)BKT- x BNZ Ceramics. *Journal of the American Ceramic Society*, 97(9):2928–2935, September 2014.

[32] E. T. Wefring, M.-a. Einarsrud, and T. Grande. Electrical conductivity and thermopower of (1x)$BiFeO_{0.5}$-x$Bi_{0.5}K_{0.5}TiO_3$ (x = 0.1, 0.2) ceramics near the ferroelectric to paraelectric. *Phys. Chem. Chem. Phys.*, 2015.

[33] K. Momma and F. Izumi. Vesta 3 for three-dimensional visualization of crystal, volumetric and morphology data. *Journal of Applied Crystallography*, 44:1272–1276, 2011.

[34] Z. F. Li, C. L. Wang, W. L. Zhong, J. C. Li, and M. L. Zhao. Dielectric Relaxor Properties of Ferroelectrics prepared by sol–gel Method. *Journal of Applied Physics*, 94(4):2548, 2003.

[35] David W Richerson. *Modern Ceramic Engineering - Properties, Processing, and Use in Design*. Taylor & Francis, 2006.

[36] Bruker AXS. Topas, 2009.

[37] T Wada, A Fukui, and Y Matsuo. Preparation of Ceramics by Polymerized Complex Method and their Properties. *Japanese Journal of Applied Physics*, 41(Part 1, No. 11B):7025–7028, November 2002.

[38] Y Hou, L Hou, S Huang, M Zhu, H Wang, and H Yan. Comparative study of nanoparticles derived from sol-gel-hydrothermal and sol-gel routes. *Solid State Communications*, 137:658–661, 2006.

[39] O. Bidault, E. Husson, and A. Morell. Effects of Lead Vacancies on the spontaneous Relaxor to Ferroelectric Phase Transition in Pb[(Mg1/3Nb2/3)0.9Ti0.1]O3. *Journal of Applied Physics*, 82(11):5674, 1997.

[40] X Chao, D Ma, R Gu, and Z Yang. Effects of CuO addition on the Electrical Responses of the low-temperature Sintered Pb(Zr2Ti0.48)O3-Pb(Mg1/3Nb2/3)O3-Pb(Zn1/3Nb2/3)O3 ceramics. *Journal of Alloys and Compounds*, 491:698–702, 2010.

[41] M Hagiwara and S Fujihara. Fabrication of dense $Bi_{0.5}K_{0.5}TiO_3$ Ceramics using hydrothermally derived fine Powders. *Journal of Materials Science*, 2015.

[42] Y. Hiruma, K. Marumo, R. Aoyagi, H. Nagata, and T. Takenaka. Ferroelectric and Piezoelectric Properties of $Bi_{0.5}K_{0.5}TiO_3$ Ceramics fabricated by hot-pressing Method. *Journal of Electroceramics*, 21(1-4):296–299, June 2007.

[43] T Wada, A Fukui, and Y Matsuo. Preparation of Ceramics by Polymerized Complex Method and their Properties. *Japanese Journal of Applied Physics*, 41(Part 1, No. 11B):7025–7028, November 2002.

[44] Y Hiruma, H Nagata, and T Takenaka. Grain-Size Effect on Electrical Properties of $Bi_{0.5}K_{0.5}TiO_3$ Ceramics. *Japanese Journal of Applied Physics*, 46(3A):1081–1084, March 2007.

[45] R. M. German, P. Suri, and S. J. Park. Review: Liquid Phase Sintering. *Journal of Materials Science*, 44(1):1–39, December 2008.